

# Rigorous Analysis of Non-Ideal Solubility of Sodium and Copper Chlorides in Water Vapor Using Pitzer-Pabalan Model

K. A. Velizhanin

*Theoretical Division, Los Alamos National Laboratory, Los Alamos, NM 87545, USA*

C. D. Alcorn, A. A. Migdisov

*Earth and Environmental Sciences, Los Alamos National Laboratory, Los Alamos, NM 87545, USA*

R. P. Currier

*Chemistry Division, Los Alamos National Laboratory, Los Alamos, NM 87545, USA*

---

## Abstract

Gaseous mixtures of water vapor and neutral molecules of salt (e.g., NaCl, CuCl etc.) can be highly non-ideal due to the strong attractive interaction between salt and water molecules. In particular, this can result in high solubility of salts in water vapor and a strong dependence of solubility on vapor pressure. The analysis of salt solubility in water vapor can be done using the Pitzer-Pabalan model, which is based on the thermodynamic theory of imperfect gases. The original Pitzer-Pabalan work demonstrated that one can reproduce experimental data for NaCl solubility in vapor. No analysis was performed on the reliability of their original fits, which we believe has contributed to the lack of applications of the Pitzer-Pabalan model despite the apparent success of the original paper. In this work, we report recent progress in developing a rigorous fitting procedure to parameterize the Pitzer-Pabalan model using experimental data. Specifically, we performed fitting of the experimental results obtained elsewhere for NaCl and CuCl. We investigate the degree of underfitting/overfitting and the sensitivity of the fitting quality to variations in the resulting fitting parameters. The results, as represented by the thermodynamic parameters describing the energetics of formation of salt-bearing water clusters, were successfully benchmarked against Gaussian 16 *ab initio* quantum chemistry calculations. The resulting rigorous fitting procedure presented here can now be applied to other systems.

---

## 1. Introduction

It is an experimental fact that a gaseous mixture of water vapor and neutral salt molecules (e.g., NaCl, CuCl etc) can be highly non-ideal with respect to the salt due to strong attractive interaction between the salt and water molecules in water vapor [1–9]. This means that the chemical potential of the salt in such equilibrium mixtures is significantly lower than it would have been, at the same concentration of salt, if water and salt molecules were not interacting. In particular, the concentration of salt in water vapor, brought to equilibrium with bulk solid salt, can be many orders of magnitude higher than the concentration of a saturated anhydrous gas in equilibrium with the solid salt. Accurate quan-

titative understanding of this non-ideality and, in particular, of this last phenomenon is very important for understanding various geological processes and for various industrial applications ranging from desalination to corrosion.

Experimental data are often represented as the concentration of salt in vapor, in equilibrium with bulk crystalline salt, measured over a range of temperatures and pressures. To make this data useful for general applications, one can generally use two approaches. The first approach is to fit the experimental data, for example, the salt concentration as a function of vapor pressure at a given temperature, by a certain empirical expression whose functional form is motivated more by ease of use than by underlying physics [6, 9, 10]. This approach is expected to work fine when interpolating experimental results. However, using this method to

---

*Email address:* kirill@lanl.gov (K. A. Velizhanin)

extrapolate experimental data to temperature and pressures beyond the ranges accessible in experiment, or to describe solubility in more complex systems (e.g., containing several gases where the density of gas mixture is not fully controlled by water vapor), can be questionable. The second, semi-empirical, approach is to fit experimental data with functional forms based on the underlying physics. For NaCl solubility in water vapor, this was done by Pitzer and Pabalan [4]. In short, their model was based on treating tightly-bound clusters made of water and salt molecules as separate molecular species. Introduction of the Gibbs free energy of formation, and its temperature derivatives, for such clusters naturally yields the concentration of salt in vapor as a function of temperature and pressure of water vapor in equilibrium. Since these Gibbs free energies are properties of a specific cluster, and do not depend on concentration of these clusters, this approach in principle allows for extrapolation to higher or lower water vapor pressures. Furthermore, since the functional form of the semi-empirical expressions for the salt concentration are based on correct physical principles, they automatically produce correct asymptotic behavior, e.g., in the case of very large or very low water vapor pressure. Extrapolation to higher and lower temperatures, beyond those covered in the experimental data, is also a possibility. The downside of the semi-empirical approach is that it yields more complicated expressions than those in the empirical approach.

In their seminal paper [4], Pitzer and Pabalan successfully fit experimental results for vapor solubility of NaCl. However, some details of the fitting procedure they used remained unexplained. For example, a single fitting variable was assigned to the enthalpy of hydration of a salt-bearing water cluster for the first three hydration steps beyond the anhydrous NaCl molecule. Another independent variable was assigned to the enthalpy of the next three hydration steps and so on. It is unknown if there was any physical motivation behind this assignment choice. Furthermore, it is unclear if (and unlikely that) this parameterization is universal enough to be able to accommodate other salts (e.g., CuCl). Finally, it is not clear whether the dependence of the enthalpy of hydration on the number of hydration steps Pitzer and Pabalan used was not overfitting the data, i.e., if the temperature and pressure ranges of experimental data, as well as the data quality (e.g. data scattering) allowed them to uniquely constrain the values of all the independent model parameters. It is a possibility that the values of enthalpies of formation they listed was only one choice of a variety of possible choices that can fit the experimental data equally well. Reliability of

the extrapolation beyond the experimental data would be questionable if this last scenario is realized. On the other hand, underfitting, where the fitting function was not flexible enough to properly fit experimental data, is also possible.

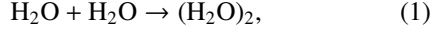
We believe that these uncertainties relating to the original work by Pitzer and Pabalan have contributed to the absence of publications where experimentally observed salt solubility in vapor were analyzed with their model. In this work, we perform a data fitting of NaCl and CuCl solubility in water vapor, obtained in previous publications [3, 4, 6, 10], analyzing rigorously (i) the degree of underfitting and overfitting, (ii) sensitivity of the fit quality to variations of fitting parameters, and (iii) what happens if some of the previously fixed model parameters are now treated as fitting variables. The last scenario is relevant in a situation where, for example, the thermodynamics of sublimation of salt is not available from thermochemical tables. Furthermore, to see whether extracted thermodynamic parameters are reasonable, we also compare them to those obtained from quantum chemical calculations performed with the Gaussian 16 software package, and also to data available from thermochemical tables.

The paper is organized as follows. The Pitzer-Pabalan model for salt solubility in water vapor is introduced in Sec. 2. To set the stage for the analysis of solubility, we first discuss the thermodynamics of pure-water and pure-salt clusters in Secs. 3 and 4, respectively. Solubilities of NaCl and CuCl in vapor are then rigorously analyzed in Secs. 5 and 6, respectively. Extracted thermodynamic parameters are discussed in Sec. 7. Our conclusions are found in Sec. 8.

## 2. Pitzer-Pabalan Model

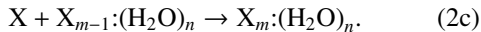
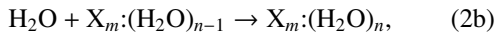
In the imperfect gas theory [11, 12], the interaction between molecules in a sufficiently dilute multicomponent molecular gas leads to the virial equation of state, where the pressure is represented as a multivariable power series in fugacities of the molecular species. It can be shown, that in the case of a strong attractive interaction between the molecules, which results in the formation of tightly bound molecular clusters, the virial coefficients of such an expansion are the equilibrium constants of formation of such clusters [11]. The virial expansion can then be reinterpreted as one corresponding to an ideal mixture of ideal gases of molecular clusters with the total pressure given by  $P = \sum_i P_i$ , where  $P_i = c_i RT$  is the partial pressure of an ideal gas of clusters of the same type (e.g., the same stoichiometry). The cluster molarities  $c_i$  are obtained from the

equilibrium constants of cluster formation and are thus determined by the strength of interaction of molecules within clusters. In other words, strong attractive interactions between molecules in a dilute gas can be treated indirectly by introducing chemical-like reactions in an otherwise ideal gas. For example, the attractive interaction between two water molecules in the water vapor can be accounted for indirectly by considering the reaction



where a new species is introduced - a tightly bound water dimer  $(\text{H}_2\text{O})_2$ . This approach belongs to the class of the so called quasi-chemical approximations [11], another example being the Hayden-O'Connell theory of dimerization [13]. The validity of the approach is based on a bound cluster being a well-defined entity, i.e., the system has to be sufficiently dilute to keep clusters spatially separated from each other. For example, the virial expansion for water vapor fails when approaching the vapor-liquid phase boundary where the density is too high to consider clusters spatially isolated and non-interacting, see Eq. (20) and the corresponding discussion below.

Pitzer and Pabalan used the imperfect gas theory together with the assumption of tightly bound clusters to describe salt solubility in water vapor [4]. They considered a gas of water and salt (e.g., NaCl or CuCl, denoted as X below) molecules in equilibrium with crystalline salt in the absence of liquid water. In the spirit of the quasi-chemical approximation, the interactions between water and salt molecules were described by the following set of reactions:



Here, Eq. (2a) describes the extraction of the single molecule of X from the solid crystalline salt  $\text{X}(\text{cr})$  into an ideal gas of single salt molecules. Typically, the gaseous salt molecule would be denoted by  $\text{X}(\text{g})$  in literature, but we omit (g) for brevity. Thus, for example,  $\text{H}_2\text{O}$  and X represent ideal gas of single water and salt molecules, respectively. A cluster made of  $m$  salt molecules and  $n$  water molecules is denoted by  $\text{X}_m:(\text{H}_2\text{O})_n$ . Accordingly, an addition of a single gaseous water or salt molecule to such a cluster is represented by Eqs. (2b) and (2c), respectively.

The changes in partial molar Gibbs free energies corresponding to Eqs. (2a)-(2c) read, respectively, as

$$\Delta G_s = G_{1,0} - G_{cr}, \quad (3a)$$

$$\Delta G_{m,n}^{(\text{H}_2\text{O})} = G_{m,n} - G_{0,1} - G_{m,n-1}, \quad (3b)$$

$$\Delta G_{m,n}^{(\text{X})} = G_{m,n} - G_{1,0} - G_{m-1,n}, \quad (3c)$$

Here, the partial molar Gibbs free energy (or molar chemical potential) of an ideal gas of clusters  $\text{X}_m:(\text{H}_2\text{O})_n$  (or in shorthand  $(m, n)$ -clusters) is denoted by  $G_{m,n}$ . The partial molar Gibbs free energy of the solid crystalline salt  $\text{X}(\text{cr})$  is denoted by  $G_{cr}$ . The Gibbs free energy of sublimation is denoted by  $\Delta G_s$ . The change of the molar Gibbs free energy in the process where a single water or salt molecule is added to a cluster to produce the  $(m, n)$ -cluster is denoted by  $\Delta G_{m,n}^{(\text{H}_2\text{O})}$  or  $\Delta G_{m,n}^{(\text{X})}$ , respectively. In what follows,  $\Delta G_{m,n}^{(\text{H}_2\text{O})}$  will be referred to as the Gibbs free energy of hydration. The set of reactions leading to the successive formation of a cluster containing a single molecule of salt, and associated changes in Gibbs free energies, are depicted in Figure 1. Some examples of formation of clusters are shown in Figure 2. The partial molar Gibbs free energy of formation of a  $(m, n)$ -cluster out of  $m$  and  $n$  gaseous molecules of salt and water, respectively, is denoted by

$$\Delta G_{m,n} = G_{m,n} - mG_{1,0} - nG_{0,1}, \quad (4)$$

where the notation is again chosen so that the pair of the subscripts in the l.h.s. denote the product species - the  $(m, n)$ -cluster. Using Eqs. (3b) and (3c),  $\Delta G_{m,n}$  can be written as a sum of energy changes corresponding to successive additions of single water and salt molecules to a cluster. For example,

$$\Delta G_{1,n} = \sum_{i=1}^n \Delta G_{1,i}^{(\text{H}_2\text{O})}, \quad (5)$$

as is illustrated in Figure 1. This allows us to write  $\Delta G_{1,n}^{(\text{H}_2\text{O})} = \Delta G_{1,n} - \Delta G_{1,n-1}$ , that is  $\Delta G_{1,n}^{(\text{H}_2\text{O})}$  can be considered a derivative of  $\Delta G_{1,n}$  with respect to  $n$ , evaluated by the finite difference method, i.e.,  $\Delta G_{1,n}^{(\text{H}_2\text{O})} \sim \frac{d(\Delta G_{1,n})}{dn}$ .

Since the gas of clusters  $\text{X}_m:(\text{H}_2\text{O})_n$  is assumed ideal, its pressure is given by

$$P_{m,n}/P^\circ = e^{(G_{m,n} - G_{m,n}^\circ)/RT}, \quad (6)$$

where  $R$  is the gas constant,  $P^\circ = 1$  bar - standard pressure, and  $G_{m,n}^\circ(T) = G_{m,n}(T, P^\circ)$  is the standard (i.e., at standard pressure, temperature is arbitrary) partial molar Gibbs free energy of the ideal gas of  $(m, n)$ -clusters. In what follows, we will generally omit writing  $T, P$  arguments unless required. In equilibrium, the l.h.s of Eqs. (3a)-(3c) vanish and one can demonstrate that  $G_{m,n} = mG_{cr} + nG_{0,1}$  expectedly holds. Substituting this into the Gibbs free energy change in Eq. (6) we obtain

$$G_{m,n} - G_{m,n}^\circ = m(G_{cr} - G_{cr}^\circ) + n(G_{0,1} - G_{0,1}^\circ) - m\Delta G_s^\circ - \Delta G_{m,n}^\circ, \quad (7)$$

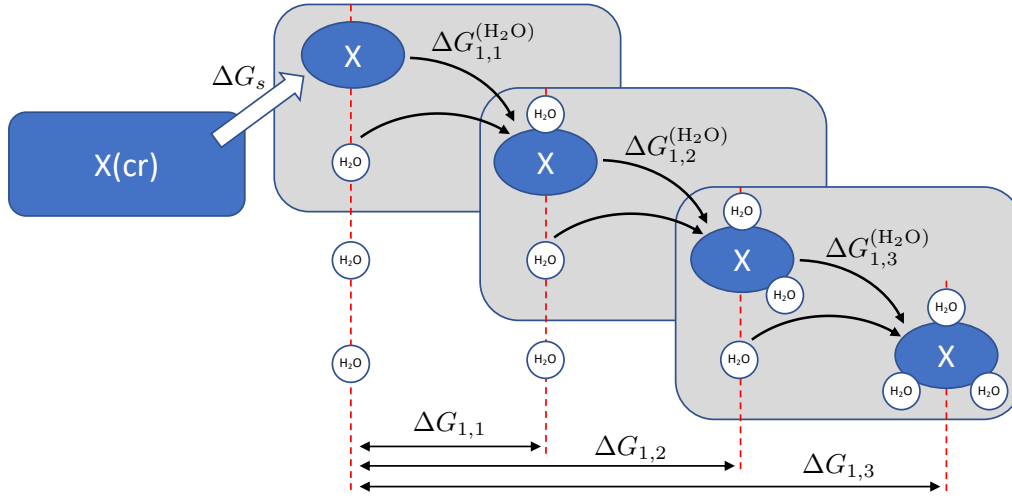


Figure 1: Schematics of successive formation of salt-bearing water cluster.

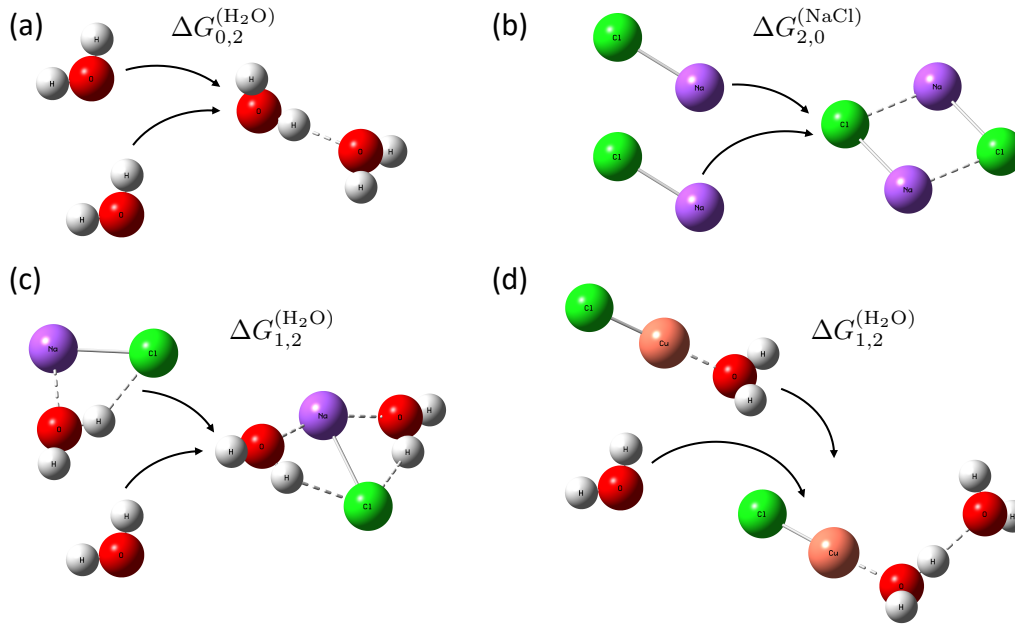


Figure 2: Several representative cluster formation processes. For each process, the change of the Gibbs free energy in the process is written. Cluster geometries are obtained from the quantum chemical calculations with the Gaussian 16 software package [14].

where  $\Delta G_{m,n}^\circ$  is given by Eq. (4), taken at the standard pressure. The fugacity of water vapor, or more simply water fugacity, is introduced as

$$f = P^\circ e^{(G_{0,1} - G_{0,1}^\circ)/RT}. \quad (8)$$

The relative activity of salt is  $a_s = e^{(G_{cr} - G_{cr}^\circ)/RT}$ . Eq. (7)

then becomes

$$G_{m,n} - G_{m,n}^\circ = mRT \ln a_s + nRT \ln \frac{f}{P^\circ} - m\Delta G_s^\circ - \Delta G_{m,n}^\circ. \quad (9)$$

Since the crystalline salt is only weakly compressible, one can assume the salt molar volume independent of pressure and apply the Poynting method to estimate the variation of  $G_{cr}(T, P)$  with pressure [15]. More specifi-

cally,  $G_{cr}(T, P) - G_{cr}^\circ(T) \approx V_s^\circ(P - P^\circ)$ , where  $P$  is the total pressure in the system and  $V_s^\circ$  is the molar volume of the crystalline salt at the standard pressure. Typical experimental pressures are up to  $P \sim 200$  bar at characteristic temperatures  $T \sim 600$  K [10]. As an example, for NaCl with an ambient density of  $2.16$  g/cm<sup>3</sup> and molar mass of  $58.4$  g/mol, the relative activity is  $a_s \approx 1.1$ . The ambient bulk modulus of NaCl is  $\sim 24$  GPa [16], which leads to relative changes of molar volume with pressure on the level of  $200 \text{ bar}/24 \text{ GPa} \sim 10^{-3}$ , thus justifying the assumption of pressure-independent molar volume. The results are very similar for CuCl. In what follows, we set  $a_s = 1$ . Therefore, Eq. (6) can be rewritten as

$$P_{m,n}/P^\circ = e^{-\Delta\tilde{G}_{m,n}^\circ/RT} \left(\frac{f}{P^\circ}\right)^n, \quad (10)$$

where  $\Delta\tilde{G}_{m,n}^\circ = m\Delta G_s^\circ + \Delta G_{m,n}^\circ$  - the change of the standard molar Gibbs free energy in a process where  $m$  salt molecules are extracted from the crystalline bulk and combined with  $n$  gaseous molecules of water to form the  $(m, n)$ -cluster. The resulting total pressure is

$$P/P^\circ = \sum'_{m,n} e^{-\Delta\tilde{G}_{m,n}^\circ/RT} \left(\frac{f}{P^\circ}\right)^n, \quad (11)$$

where the primed sum means that summation is done over all pairs  $m, n \geq 0$  that satisfy  $m + n > 0$ . In particular, we can write

$$P/P^\circ = \sum_{n=1}^{\infty} e^{-\Delta G_{0,n}^\circ/RT} \left(\frac{f}{P^\circ}\right)^n + \sum_{n=0}^{\infty} e^{-\Delta\tilde{G}_{1,n}^\circ/RT} \left(\frac{f}{P^\circ}\right)^n + \dots, \quad (12)$$

where the first r.h.s term corresponds to imperfect water vapor with no salt in it. Instead of explicitly performing the summation in this term, we use a Python implementation of IAPWS-95 - an accurate equation of state (EOS) for water vapor [17, 18]. The second r.h.s. term represents  $(1, n)$ -clusters. We will demonstrate below, in Sec. 4.1, that only these two terms are important for conditions considered in this work, or in other words, contributions from clusters bearing two or more salt molecules are negligible. Under these conditions, the partial pressure of the salt-bearing clusters is

$$P_X/P^\circ = \sum_{n=0}^{\infty} e^{-\Delta\tilde{G}_{1,n}^\circ/RT} \left(\frac{f}{P^\circ}\right)^n. \quad (13)$$

Here, each summation term is proportional to the concentration of the cluster of the corresponding size. The

mean number of water molecules in a cluster can, therefore, be calculated as

$$\langle n \rangle = \frac{\sum_{n=0}^{\infty} n e^{-\Delta\tilde{G}_{1,n}^\circ/RT} \left(\frac{f}{P^\circ}\right)^n}{\sum_{n=0}^{\infty} e^{-\Delta\tilde{G}_{1,n}^\circ/RT} \left(\frac{f}{P^\circ}\right)^n} = \frac{\partial \ln P_X}{\partial \ln f}. \quad (14)$$

Values of  $\Delta\tilde{G}_{1,n}^\circ$  are functions of temperature, and in order to obtain them from fits to experimental data, we need to approximate them with a few-parameter functional form. As in Ref. [4], we assume that the constant-pressure heat capacities, defined by the second derivative of  $\Delta\tilde{G}_{1,n}^\circ$  with respect to temperature, are temperature-independent constants. This results in

$$\Delta\tilde{G}_{1,n}^\circ(T) = \Delta\tilde{H}_{1,n}^\circ - T\Delta\tilde{S}_{1,n}^\circ - T\Delta\tilde{C}_{1,n}^\circ \left[ \ln \frac{T}{T_{\text{ref}}} + \frac{T_{\text{ref}}}{T} - 1 \right], \quad (15)$$

where the three parameters  $\Delta\tilde{H}_{1,n}^\circ$ ,  $\Delta\tilde{S}_{1,n}^\circ$  and  $\Delta\tilde{C}_{1,n}^\circ$  are the molar enthalpy, entropy and constant-pressure heat capacity changes for the process of formation of  $(1, n)$ -cluster out of  $n$  gaseous water molecules and a salt molecule, extracted from bulk, evaluated at the standard pressure  $P^\circ$  and the reference temperature  $T_{\text{ref}}$ . To facilitate comparison with results of Ref. [4], the reference temperature is taken  $T_{\text{ref}} = 500$  K. We emphasize again that superscript  $\circ$  stands for the standard state at the standard pressure ( $P^\circ = 1$  bar), but arbitrary temperature, whereas superscript  $\ominus$  also sets the temperature to be  $T = T_{\text{ref}}$ . In this paper,  $C$  denotes the constant-pressure molar heat capacity. We, therefore, omit  $P$  in the usual notation  $C_P$  for brevity. Expressions analogous to Eq. (15) will also be used to represent the temperature dependence of  $\Delta G_s^\circ$ ,  $\Delta G_{1,n}^\circ$ ,  $\Delta G_{1,n}^{\circ(X)}$  and  $\Delta G_{1,n}^{\circ(\text{H}_2\text{O})}$ . The accuracy of assuming a temperature-independent heat capacity in Eq. (15) will be discussed in Sec. 7.4.

### 3. Thermodynamics of $(\text{H}_2\text{O})_n$ cluster formation

In this and the following section, we discuss the thermodynamics of forming pure-water and pure-salt clusters, respectively. Primarily, we do this because we expect that the thermodynamics of forming salt-bearing water clusters will be somewhere ‘‘in between’’ those of pure-water and pure-salt. Secondary, since good quality experimental data is available for thermodynamics of pure clusters, it can serve as a benchmark for the reliability of the quantum chemistry-based calculations.

First, consider the process of forming large water clusters, Eq. (2b) at  $m = 0$  and  $n \gg 1$ . It turns out

that the complete thermodynamic description of such a process can be extracted from a complete EOS that describes both vapor and liquid water. The black line in Figure 3 shows the dependence of the molar Gibbs free energy for water at  $T = T_{\text{ref}}$ , evaluated from the IAPWS-95 EOS [17, 18].

At this temperature, liquid water is a thermodynamically stable phase at  $P \gtrsim 28$  bar, with vapor being stable at lower pressures. The vapor-liquid phase transition appears as a derivative discontinuity in the black line. To obtain the thermodynamic parameters for a process involving addition of a single water molecule to a large pure-water cluster, we first consider the thermodynamics of the ideal vapor. According to the first r.h.s term in Eq. (12), the vapor becomes ideal (i.e., no water clusters, just monomers) at infinitely low pressures. In practice, we assume that the vapor is sufficiently ideal at some low pressure  $P'$  (e.g.,  $\sim 10^{-3}$  bar). The partial molar Gibbs free energy for the ideal vapor at arbitrary pressure  $P$  is then evaluated as

$$G_{0,1}(T, P) = G(T, P') + RT \ln P/P', \quad (16)$$

where  $G(T, P')$  is calculated directly from IAPWS-95 and other thermodynamic state functions are obtained from  $G_{0,1}(T, P)$  using thermodynamic derivatives. The resulting Gibbs free energy, entropy and heat capacity of the ideal vapor are plotted as dashed blue lines in Figure 3(a), (b) and (c), respectively. That  $P'$  was taken sufficiently low is confirmed by, for example, panel (a) where the dashed blue line agrees perfectly with IAPWS-95 at low pressures. Close to the boiling point (e.g.,  $P \sim 20$  bar), the Gibbs free energy of the real vapor deviates from ideality due to the contribution of dimers and larger clusters. As an illustration to using thermodynamic derivatives to obtain various thermodynamic parameters from Eq. (16), the dependence of constant-pressure heat capacity for the ideal vapor (i.e., the gas of monomers) at standard pressure, computed from the second derivative of  $G_{0,1}$  with respect to temperature, is represented by the black line in Figure 4.

Now consider an ideal gas of very large salt-free water clusters ( $m = 0, n \gg 1$ ). Each such cluster can be treated as a droplet of liquid water [19–21] and therefore the partial Gibbs free energy for a mole of large  $(0, n)$ -clusters can be written as

$$G_{0,n}^{\circ}(T) \approx nG_{\text{liq}}(T), \quad (17)$$

where  $G_{\text{liq}}(T)$  is the Gibbs free energy of a mole of water molecules in the liquid phase. We neglected the contributions of translation and rotation of the cluster as the

whole, as well as the surface energy term, in the r.h.s. of Eq. (17), since they are small compared to  $nG_{\text{liq}}$  for sufficiently large clusters [20]. An important point is that since the imperfect gas theory assumes that clusters do not interact directly,  $G_{\text{liq}}$  has to be evaluated at zero pressure, and not at  $P^{\circ}$ . Thermodynamic information for liquid water at zero pressure is not directly available since the liquid water is not a thermodynamically stable phase at zero pressure. However, thermodynamic variables are seen to vary slowly with pressure in Figure 3 in the liquid regime ( $P \gtrsim 28$  bar), which is the result of the very low compressibility of liquid water. We can thus extrapolate thermodynamic state functions, evaluated where the liquid phase is still stable, to zero pressure using, for example, a low-degree polynomial regression. This approach yields thermodynamic properties of a metastable phase - the liquid water at zero pressure. The constant-pressure heat capacity of liquid water, extracted by this method and normalized to a mole of water molecules, is represented by the blue line in Figure 4.

Using Eq. (17), the change in the molar Gibbs free energy in the process of adding a water molecule to a large  $(0, n)$ -cluster can be calculated as

$$\Delta G_{0,n}^{\circ(\text{H}_2\text{O})} = G_{0,n}^{\circ} - G_{0,1}^{\circ} - G_{0,n-1}^{\circ} = G_{\text{liq}} - G_{0,1}^{\circ}. \quad (18)$$

Temperature derivatives of this expression produce the enthalpy, entropy and constant-pressure heat capacity changes,  $\Delta H_{0,\infty}^{\circ}$ ,  $\Delta S_{0,\infty}^{\circ}$  and  $\Delta C_{0,\infty}^{\circ}$  ( $n$  is substituted with  $\infty$  to emphasize the large size of clusters), plotted in Figure 5 by the blue lines. Corresponding changes in standard molar enthalpy, entropy and constant-pressure heat capacity at the reference temperature are shown in the last row of Table 1. These three parameters can be used in an equation similar to Eq. (15) to approximate the temperature dependence of  $\Delta G_{0,\infty}^{\circ(\text{H}_2\text{O})}$ .

It is instructive to attempt to use Eq. (17) in order to calculate the pressure of pure water vapor from Eq. (12) in the large fugacity regime where the contribution of large water clusters to the total pressure is expected to be dominant. To this end, we substitute Eqs. (4) and (17) into the first r.h.s term of Eq. (12) to obtain

$$\begin{aligned} P_{\text{H}_2\text{O}} &= P^{\circ} \sum_{n=1}^{\infty} e^{-\Delta G_{0,n}^{\circ}/RT} \left( \frac{f}{P^{\circ}} \right)^n \\ &\approx P^{\circ} \sum_{n=1}^{\infty} e^{-n(G_{\text{liq}} - G_{0,1}^{\circ})/RT} \left( \frac{f}{P^{\circ}} \right)^n. \end{aligned} \quad (19)$$

This constitutes an infinite geometric series which can be summed up exactly to yield, with the help of Eq. (8)

$$P_{\text{H}_2\text{O}} = P^{\circ} \left[ e^{(G_{\text{liq}} - G_{0,1}^{\circ})/RT} - 1 \right]^{-1}. \quad (20)$$

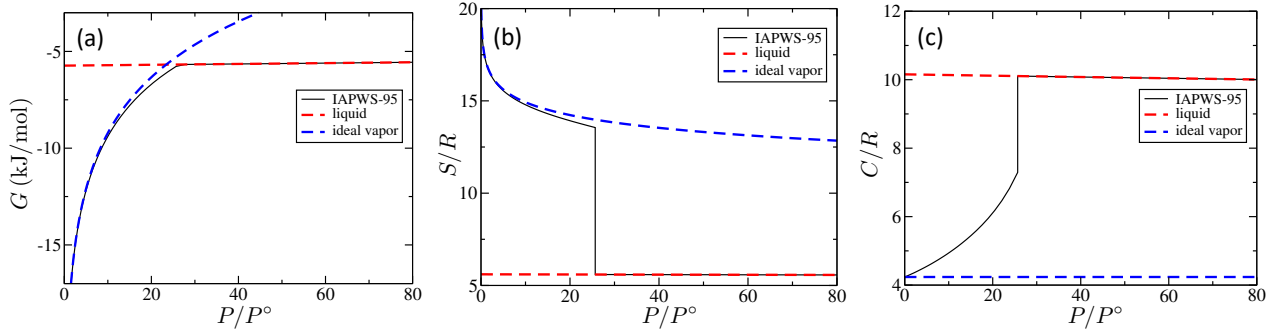


Figure 3: Molar Gibbs free energy, entropy and constant-pressure heat capacity for water (IAPWS-95 EOS) are plotted as functions of pressure at  $T = T_{\text{ref}}$ .

	$\Delta H_{0,n}^{\circ}(\text{H}_2\text{O})$ (kJ/mol)	$\Delta S_{0,n}^{\circ}(\text{H}_2\text{O})/R$	$\Delta C_{0,n}^{\circ}(\text{H}_2\text{O})/R$
$n = 2$	-16.59	-9.49	-2.51
$n = \infty$	-35.26	-11.62	5.92

Table 1: Standard molar enthalpy, entropy and heat capacity of hydration of pure-water clusters, evaluated from IAPWS-95 at  $T_{\text{ref}}$ .

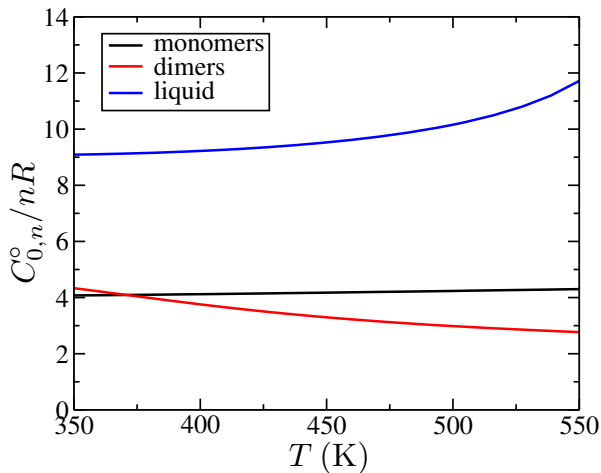


Figure 4: Molar constant-pressure heat capacities extracted from IAPWS-95 for ideal gas of monomers ( $n = 1$ ), dimers ( $n = 2$ ) and very large clusters ( $n = \infty$ ) at standard pressure. Heat capacities are normalized per mole of water molecules,  $C_{0,n}^{\circ}/nR$ .

The pressure of water vapor is thus seen to monotonically increase when the partial molar Gibbs free energy of ideal water vapor approaches that of liquid water from below. The pressure diverges, indicating the limit of applicability of the virial expansion in Eq. (19), at  $G_{0,1} = G_{\text{liq}}$ , which is the vapor-liquid phase boundary.

### 3.1. Water dimer formation

Now consider the formation of the smallest possible pure-water clusters, i.e., dimers. As discussed above,

the deviation of the Gibbs free energy for water from that of ideal vapor (black and dashed blue lines, respectively, in Figure 3(a)), at pressures just below the boiling point ( $P \lesssim 28$  bar) is due to the non-ideality of water vapor. The pressure of non-ideal vapor can be approximated by truncating the summation in the first r.h.s term of Eq. (12) to only monomers and dimers, resulting in  $P \approx f + e^{-\Delta G_{0,2}^{\circ}/RT} f^2/P^{\circ}$ . Here, the fugacity  $f$  of the non-ideal vapor is exactly the pressure of the ideal vapor at the same Gibbs free energy, and so one can extract  $\Delta G_{0,2}^{\circ} = \Delta G_{0,2}^{\circ}(\text{H}_2\text{O})$  by evaluating the low-pressure limit of  $(P_{\text{steam}} - f)/f^2$  from the difference between the solid black and dashed blue lines in Figure 3(a). The low-pressure limit is required to eliminate the contribution of trimers and larger clusters. Finding  $\Delta G_{0,2}^{\circ}$  as a function of temperature and numerically evaluating its temperature derivatives provides the changes in other thermodynamic parameters for the same process. Standard molar enthalpy, entropy and heat capacity changes, extracted from IAPWS-95 using this approach, are shown in Figure 5 by the black lines. Standard molar enthalpy, entropy and heat capacity changes evaluated at  $T_{\text{ref}}$  are given in the upper numerical row of Table 1. The temperature dependence of heat capacity for a water molecule in the dimer is depicted in Figure 4 by the red line. Essentially the same approach, also based on IAPWS-95, was used in Ref. [22]. Two representative temperature points from this reference are shown in Figure 5 by green circles.

To have an independent source of thermodynamic parameters for the cluster formation processes, we per-

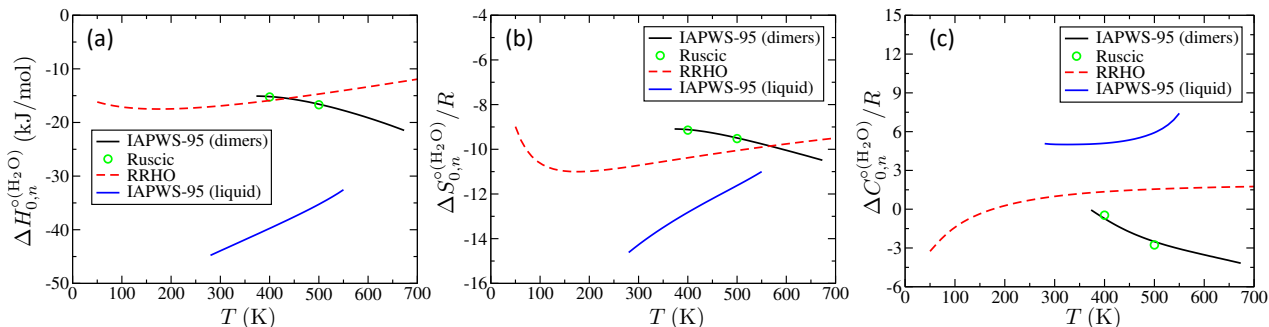


Figure 5: Standard molar enthalpy, entropy and heat capacity of hydration of pure-water clusters are plotted as functions of temperature in panels (a), (b) and (c), respectively. Thermodynamic parameters for dimer formation, extracted from IAPWS-95 in this work and adopted from Ref. [22], are shown by the black lines and green circles, respectively. The corresponding results of quantum chemical calculations are given by the dashed red lines. The thermodynamics of a single hydration step of a very large pure-water cluster is represented by the blue lines.

formed quantum chemical calculations using the Gaussian 16 software package [14]. The computational method used was Density Functional Theory [23], performed with the B3LYP [24, 25] functional and a 6-311+G(d,p) basis set for all atoms. Structural optimizations and vibrational calculations were all performed at this level. The grid used for numerical integration of exchange-correlation energies was ultrafine, and the spatial step-size during optimization was held as small as possible. Chloride complexes and water clusters were explicitly hydrated by building up structures one water molecule at a time. For example, the lowest energy structure for  $X:(H_2O)_n$  was found by placing an explicit water molecule at several orientations (5 – 15) around the  $X:(H_2O)_{n-1}$  cluster, and allowing each of these initial guesses to optimize independently. The  $X:(H_2O)_n$  structure with the lowest “cold” energy (energy at  $T = 0$  with zero-point energies of vibrations excluded) was then chosen, and used to construct the initial guesses for  $X:(H_2O)_{n+1}$ . This approach samples many possible geometries and maximizes the chances of finding the true global minimum for a given cluster. All optimizations were confirmed to be at an energy minima by a subsequent vibrational calculation that resulted in no imaginary frequencies.

The total ground-state energy of a cluster in its optimal geometry, the moment of inertia tensor and the vibrational frequencies were extracted from Gaussian 16 output files. These parameters were then used to generate a complete internally consistent EOS for an ideal gas of clusters of a given size within the rigid rotor harmonic oscillator (RRHO) approximation [26] using the code Magpie [27]. The ground electronic state was always assumed. Such thermochemical calculations are illustrated in Figure 5, where the standard molar en-

thalpy, entropy and heat capacity changes, corresponding to the formation of a water dimer, Eq. (1), are shown by the dashed red lines in panels (a), (b) and (c), respectively. As one can see, the magnitudes of enthalpy and entropy changes for the dimer formation process, obtained using the two described methods, agree reasonably well. Their temperature dependences and therefore the change in heat capacity are rather different however. In particular,  $\Delta C_{0,2}^{o(H_2O)}$  is of different sign for RRHO and IAPWS-95 based approaches. This disagreement is likely originating from the well-known failure of RRHO to account for the anharmonicity of the low-frequency inter-molecular vibrations [22].

#### 4. Thermodynamics of $X_m$ cluster formation

Now consider dimerization of NaCl molecules in an anhydrous vapor of sodium chloride. RRHO results for this process are shown by dashed red lines in Figure 6. Thermochemical data for NaCl monomers, dimers and crystalline bulk are available from the JANAF thermochemical tables [28]. This allows one to evaluate the thermodynamics of formation of dimers and very large clusters out of the ideal gas of monomers. The former, plotted by solid black lines in Figure 6, shows the reasonable agreement with the RRHO results for the enthalpy and entropy, and good agreement for the heat capacity.

The thermodynamics for the process of adding a NaCl monomer to a large cluster, Eq. (2c) with  $m \gg 1$  and  $n = 0$ , is shown by the blue lines in the same figure. The caveat is that since the thermodynamic data for NaCl is only available at standard pressure from the tables, one cannot extrapolate to zero pressure as we did for large pure-water clusters. However, the compressibility of crystalline NaCl is lower than that of liquid



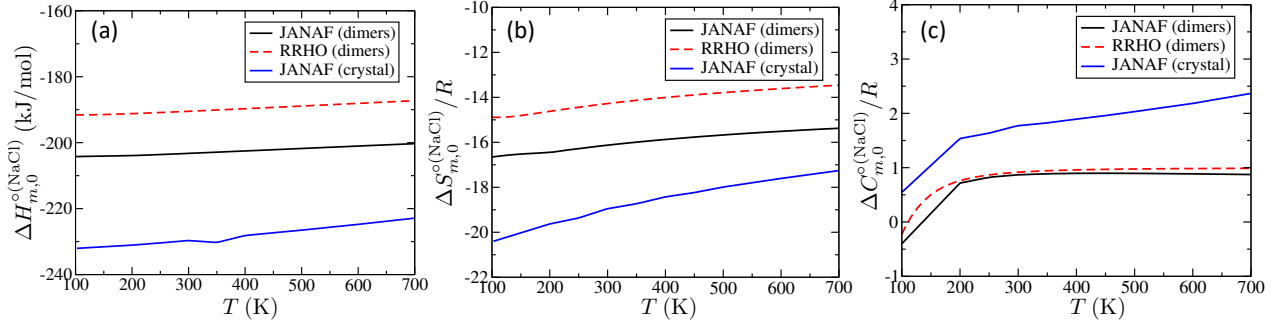


Figure 6:  $\Delta H_{m,0}^{o(\text{NaCl})}$ ,  $\Delta S_{m,0}^{o(\text{NaCl})}$  and  $\Delta C_{m,0}^{o(\text{NaCl})}$  for the process of addition of a NaCl monomer to a pure NaCl cluster, Eq. (2c) at  $n = 0$ . Thermodynamic state functions are extracted from JANAF tables for  $m = 2$  (black lines), and  $m = \infty$  (blue lines). RRHO results for the dimer formation ( $m = 2$ ) are represented by the dashed red lines.

water by at least an order of magnitude so we simply assume that the bulk NaCl thermodynamics potentials are the same at zero and standard pressures. It is expected that an added monomer interacts with more salt molecules in a larger cluster than in a dimer, which rationalizes the observation of  $\Delta H_{\infty,0}^{o(\text{NaCl})} < \Delta H_{2,0}^{o(\text{NaCl})}$  and  $\Delta C_{\infty,0}^{o(\text{NaCl})} > \Delta C_{2,0}^{o(\text{NaCl})}$  in the figure. On the other hand, the motion of salt molecules in the large cluster is more correlated than in the dimer due to the stronger interaction in the former case, which is the reason for  $\Delta S_{\infty,0}^{o(\text{NaCl})} < \Delta S_{2,0}^{o(\text{NaCl})}$  in Figure 6(b).

The knowledge of the dimer formation thermodynamics allows one to estimate the contribution of  $(2, n)$ -clusters to  $P_X$ . Eq. (10) yields  $P_{2,n}/P^\circ = e^{-\Delta\tilde{G}_{2,n}^\circ/RT} \left(\frac{f}{P^\circ}\right)^n$ , where

$$\begin{aligned} \Delta\tilde{G}_{2,n}^\circ &= 2\Delta G_s^\circ + \Delta G_{2,0}^{o(\text{NaCl})} + \Delta G_{2,1}^{o(\text{H}_2\text{O})} \\ &+ \Delta G_{2,2}^{o(\text{H}_2\text{O})} + \dots + \Delta G_{2,n}^{o(\text{H}_2\text{O})}. \end{aligned} \quad (21)$$

The last  $n$  r.h.s. terms in this expression describe the successive addition of water molecules to the NaCl dimer, stabilizing the latter. The stabilization effect is expected to be greater for a single NaCl molecule than for the dimer because in the latter case the interaction between a salt molecule and water is screened by the other salt molecule. We can therefore estimate  $P_{2,n}$  from above by substituting  $\Delta G_{2,i}^{o(\text{H}_2\text{O})}$  with  $\Delta G_{1,i}^{o(\text{H}_2\text{O})}$ , which transforms Eq. (21) into

$$\Delta\tilde{G}_{2,n}^\circ \approx \Delta G_s^\circ + \Delta G_{2,0}^{o(\text{NaCl})} + \Delta\tilde{G}_{1,n}^\circ \quad (22)$$

which in turn produces

$$P_{2,n}/P^\circ \approx e^{-[\Delta G_s^\circ + \Delta G_{2,0}^{o(\text{NaCl})}]/RT} P_{1,n}/P^\circ. \quad (23)$$

We estimate the value of the exponential function in the r.h.s. of Eq. (23) at  $T_{\text{ref}}$  using the data from Figure 6 and Table 2 to be  $\approx 0.01$  so  $P_{2,n}$  is smaller than

$0.01P_{1,n}$ . Therefore, the NaCl solubility in water vapor is strongly dominated by  $(1, n)$ -clusters. We expect this statement to be accurate at other temperatures, as well as for CuCl. The one caveat in the above considerations is that it is assumed that two salt monomers are bonded inside a water cluster. However, if there is large water cluster formed (effectively a droplet of liquid water), there is a gain in translational entropy if the salt dimer is split into two monomers that can explore the volume of the droplet independently. Furthermore, dissociation of neutral salt monomers into atomic ions can be expected in such droplets. This is expected to become important only very close to the vapor-liquid phase transition, i.e., for highly non-ideal vapor containing a lot of droplets. We do not consider this regime here.

Assuming classical harmonic intra- and intermolecular vibrations, the molar heat capacity of an ideal gas of NaCl monomers is  $C_{1,0}^\circ = \frac{3}{2}R + \frac{2}{2}R + \frac{1}{1}R + R$ , where the r.h.s. terms stand for, respectively, the contributions of three translational degrees of freedom (DOF), the rotation of a linear rotor, the single vibrational mode, and the difference between constant-volume and constant-pressure heat capacities of an ideal gas. This results in  $C_{1,0}^\circ/R = 4.5$ . For a dimer, and larger clusters, similar considerations yield (assuming a non-linear rotor)  $C_{m,0}^\circ = \frac{3}{2}R + \frac{3}{2}R + \frac{6m-6}{1}R + R = (6m-2)R$ , which results in  $C_{2,0}^\circ/2R = 5$  and  $C_{m,0}^\circ/mR = 6R$  for  $m \rightarrow \infty$ . These simple estimates are seen to agree well with results calculated from the JANAF tables [28] in Figure 7. Some deviations are due to anharmonicity in large clusters and partially quantum-mechanically “frozen” vibrational modes in small clusters. The changes in heat capacities as  $\Delta C_{m,0}^{o(\text{NaCl})} = C_{m,0}^\circ - C_{m-1,0}^\circ - C_{1,0}^{o(\text{NaCl})}$  result in the solid black and blue lines in Figure 6(c). The agreement of the RRHO results for the dimer with the black line is also good, implying that the assumption of har-

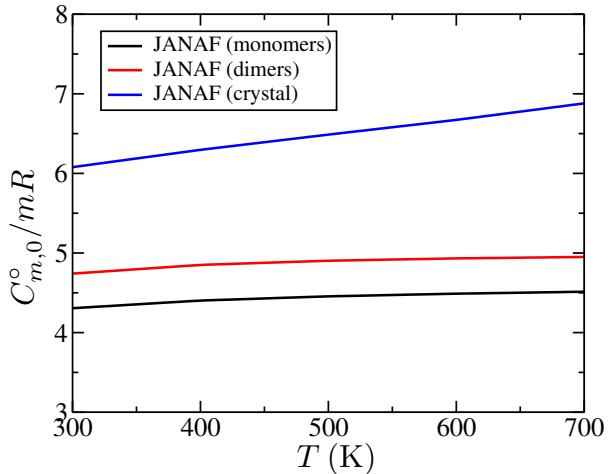


Figure 7: Standard molar heat capacity of a pure-NaCl cluster normalized per number of salt monomers in it,  $C_{m,0}^{\circ}/mR$ . The results for monomers ( $m = 1$ ), dimers ( $m = 2$ ) and crystalline phase ( $m \rightarrow \infty$ ) are plotted by the black, red and blue lines, respectively.

monic vibrations in RRHO is accurate in small clusters.

An application of the same DOF-counting approach to evaluation of heat capacities of pure-water clusters produces

$$C_{0,n}^{\circ} = \frac{3}{2}R + \frac{3}{2}R + \frac{6n-6}{1}R + R, \quad (24)$$

where the inter-molecular vibrations ( $6n - 6$  DOFs) are all assumed classical and harmonic, and the intra-molecular vibrations are all assumed quantum-mechanically frozen and, therefore, not contributing to the heat capacity. The results are  $C_{0,1}^{\circ}/R = 4$ ,  $C_{0,2}^{\circ}/2R = 5$  and  $C_{0,n}^{\circ}/nR = 6$  for  $n \rightarrow \infty$ . These could be compared to the results extracted from IAPWS-95, Figure 4. The agreement is good for the ideal gas of monomers. The agreement is worse for the dimers and, especially, for the very large clusters. The difference is expected to be due to significant anharmonicity of van der Waals interaction between water molecules in clusters. The same anharmonicity is the chief reason for disagreement between IAPWS-95 and RRHO results for dimers in Figure 5.

The thermodynamics of successive addition of water molecules to a salt-bearing water cluster  $X:(H_2O)_n$  should converge to that of pure-water clusters at large  $n$ . The above considerations of heat capacities demonstrated that the thermodynamics of water clusters is complex so, for example, simple estimates of the cluster heat capacities based on counting DOFs are inaccurate. We postulate that the agreement between such simple estimates and experimental data for heat capacities of

$X:(H_2O)_n$  in Ref. [4] are due to error cancellation.

#### 4.1. Thermodynamics of sublimation

Thermodynamics of sublimation for NaCl and CuCl is known accurately from the JANAF [28] and Pankratz [29] thermochemical tables. In particular,  $\Delta G_s^{\circ}(T)$  can be extracted from the tables over a wide temperature range. However, (i) to treat all the thermochemical data on the same level of approximations, and also (ii) to anticipate situations where such detailed thermochemical data on temperature variation is not available, we will use an expression similar to Eq. (15) to represent  $\Delta G_s^{\circ}(T)$  instead of the full thermochemical data. To properly parameterize such an expression, we first generate  $P_X(T)$  from Eq. (13) at vanishing water fugacity over an experimentally realistic temperature range using the full thermochemical data from the JANAF [28] and Pankratz [29] tables. Then, the resulting  $P_X(T)$  is fit with the combination of Eq. (13) and Eq. (15). The fitting procedure will be described in detail in Sec. 5.1. The results of the fitting are compiled in Table 2, and the fit qualities can be seen in Figure 8. Pressure evaluated directly from the thermochemical tables is shown in Figure 8 by solid lines. The fitting results are shown by black dots and magenta circles. The agreement is excellent for both NaCl and CuCl, even though Eq. (15) is a smooth function of temperature, and, therefore, might not *a priori* be considered applicable to describe the thermodynamics of CuCl, which has a solid-to-liquid transition at  $T \approx 700$  K. In Table 2, the first four numerical columns represent the fitting of NaCl and CuCl sublimation thermodynamics, with thermochemical data coming Refs. [28, 29], where all the three parameters  $\Delta H_s^{\circ}$ ,  $\Delta S_s^{\circ}$  and  $\Delta C_s^{\circ}$  are allowed to vary. These results are shown by black dots in the Figure. As is seen in Table 2, fitting the Pankratz thermochemical data for CuCl results in a significantly larger magnitude of the change in the heat capacity upon sublimation (fourth numerical column), compared to those in the first three numerical columns. To test the sensitivity of the fitting quality to this parameter, we also fit the same thermochemical data with the constraint  $\Delta C_s^{\circ}/R = -3$ . The result of this fit, the last column in Table 2, is represented by magenta circles in Figure 8. The deviation from the direct thermochemical data, and from the fit with all the three parameter varied, is almost negligible, indicating that the magnitude of  $\Delta C_s^{\circ}$  extracted from this fitting is not too reliable.

The condensation of gaseous NaCl into a crystal (i.e., reverse sublimation) can be thought of as adding a single salt molecule to a very large NaCl cluster, i.e., we expect  $\Delta G_s^{\circ} = -\Delta G_{\infty,0}^{\circ(\text{NaCl})}$ , and similarly for  $\Delta H^{\circ}$  and

	NaCl (J)	NaCl (P)	CuCl (J)	CuCl (P)	CuCl (P)
$\Delta H_s^\circ$ (kJ/mol)	227	231	225	243	239
$\Delta S_s^\circ/R$	18.0	18.0	16.9	17.0	15.5
$\Delta C_s^\circ/R$	-2.28	-2.31	-2.97	-7.59	-3 (forced)

Table 2: Standard molar enthalpy, entropy and heat capacity of sublimation, Eq. (2a), obtained from fitting the solid lines in Figure 8. (J) and (P) stand for the JANAF [28] and Pankratz [29] thermochemical tables. The last column corresponds to fitting where the heat capacity of sublimation was forced to be  $\Delta C_s^\circ/R = -3$  when fitting.

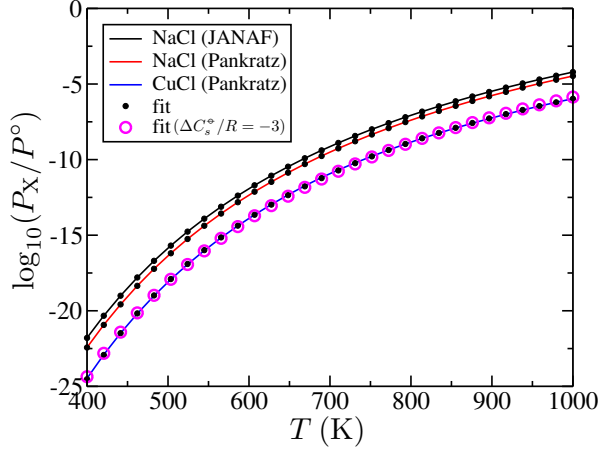


Figure 8: Pressure of anhydrous NaCl and CuCl monomer vapors in equilibrium with crystalline NaCl and CuCl, respectively, as a function of temperature. The data obtained from the JANAF [28] and Pankratz [29] thermochemical tables are depicted by solid lines. Black dots represent the fitting results where the enthalpy, entropy and heat capacity of sublimation were all allowed to vary. Magenta circles depict the fitting result where only the enthalpy and entropy of sublimation were allowed to vary, but the heat capacity of sublimation was set to  $\Delta C_s^\circ/R = -3$ .

$\Delta S^\circ$ . It is thus instructive to compare the thermodynamics of reverse sublimation (values in Table 2 taken with the opposite sign) to that of formation of NaCl dimer. In particular, salt molecules in a dimer are expected to interact more loosely than in bulk, which should result in  $\Delta H_{2,0}^{\circ(\text{NaCl})} > -\Delta H_s^\circ$ , and  $\Delta S_{2,0}^{\circ(\text{NaCl})} > -\Delta S_s^\circ$ . Comparing Figure 6 and Table 2 we see that  $\Delta H^{\circ(\text{NaCl})}$  and  $\Delta S^{\circ(\text{NaCl})}$  are indeed larger for the dimer than for bulk, although not by much.

## 5. Solubility of Sodium Chloride in Water Vapor

In their seminal paper [4], Pitzer and Pabalan were able to reproduce various experimental data for NaCl solubility in water vapor using the imperfect gas theory outlined above. The enthalpy, entropy and heat capacity changes, obtained for successive addition of water molecules to a cluster, are given in the first, third and

fourth numerical columns, respectively, of Table 3. In order to reproduce the Pitzer-Pabalan modeling results we needed to slightly modify some of their originally reported enthalpies. We suspect that the values were rounded off too coarsely in Table 2 of the original publication [4]. The new corrected enthalpies are given in the second numerical column of Table 3. The parameters from the second, third and fourth numerical columns of the table are plotted by black dots in panels (b), (c) and (d), respectively, of Figure 9. Using these corrected values (entropy and heat capacity values are left the same), along with those in the first column of Table 2 to calculate  $\Delta G_s^\circ(T)$ , we reproduced Pitzer and Pabalan's results for the partial pressure of NaCl-bearing water clusters. In particular, the dependence of  $P_{\text{NaCl}}$  on water fugacity, Eq. (13), for three different temperatures is depicted in Figure 9(a) by the solid lines. Results at  $T = 450^\circ\text{C}$  from Figure 2 in Ref. [4] are plotted as black dots in Figure 9(a). As can be seen, it agrees perfectly with what is calculated in this work using the corrected values of thermodynamic parameters (blue line). To explore questions related to possible overfitting,  $P_{\text{NaCl}}$  dependences on  $f$  for a range of temperatures were generated from the Pitzer-Pabalan model using the parameters given in the last three columns of Table 3. Those data, treated as if they were experimental results, were then used to test the model developed in this work. This approach allows for a direct comparison with the original Pitzer-Pabalan results, see e.g., Figure 10(b) below.

The dependence of  $P_{\text{NaCl}}$  on temperature (at fixed  $f$ ) is qualitative different at lower and higher fugacities as seen in Figure 9. The temperature derivative of Eq. (9) is

$$\left(\frac{\partial P_X}{\partial T}\right)_f = P^\circ \sum_{n=0}^{\infty} \frac{\Delta \tilde{H}_{1,n}^\circ}{RT^2} e^{-\Delta \tilde{G}_{1,n}^\circ/RT} \left(\frac{f}{P^\circ}\right)^n, \quad (25)$$

where, as defined above,  $\Delta \tilde{H}_{1,n}^\circ = \Delta H_s^\circ + \Delta H_{1,1}^{\circ(\text{H}_2\text{O})} + \Delta H_{1,2}^{\circ(\text{H}_2\text{O})} + \dots + \Delta H_{1,n}^{\circ(\text{H}_2\text{O})}$ . For clusters with a small number of water molecules, this sum is dominated by a large positive  $\Delta H_s^\circ$ , yielding  $\Delta \tilde{H}_{1,n}^\circ > 0$ . On the other hand,  $\Delta H_{1,n}^{\circ(\text{H}_2\text{O})}$  are negative due to the exothermicity of hy-

	$\Delta H_{1,n}^{\ominus(\text{H}_2\text{O})}$ (kJ/mol)	$\Delta H_{1,n}^{\ominus(\text{H}_2\text{O})}$ (kJ/mol), corrected	$\Delta S_{1,n}^{\ominus(\text{H}_2\text{O})}/R$	$\Delta C_{1,n}^{\ominus(\text{H}_2\text{O})}/R$
$n = 1 - 3$	-53.1	-53.1	-11	3
$n = 4 - 6$	-40.7	-40.7		
$n = 7 - 9$	-35.8	-35.6		
$n = 10 - \infty$	$-32.8 + 0.42 \times \text{floor}\left(\frac{n-10}{3}\right)$	$-32.6 + 0.58 \times \text{floor}\left(\frac{n-10}{3}\right)$		

Table 3: Thermodynamic parameters of hydration of salt-bearing water clusters for the original Pitzer-Pabalan model [4]. First numerical column is original enthalpies from Ref. [4]. The floor function is denoted by floor(). Second numerical column is the corrected version of the first column. The last two columns are  $n$ -independent standard molar entropy and heat capacity of hydration.

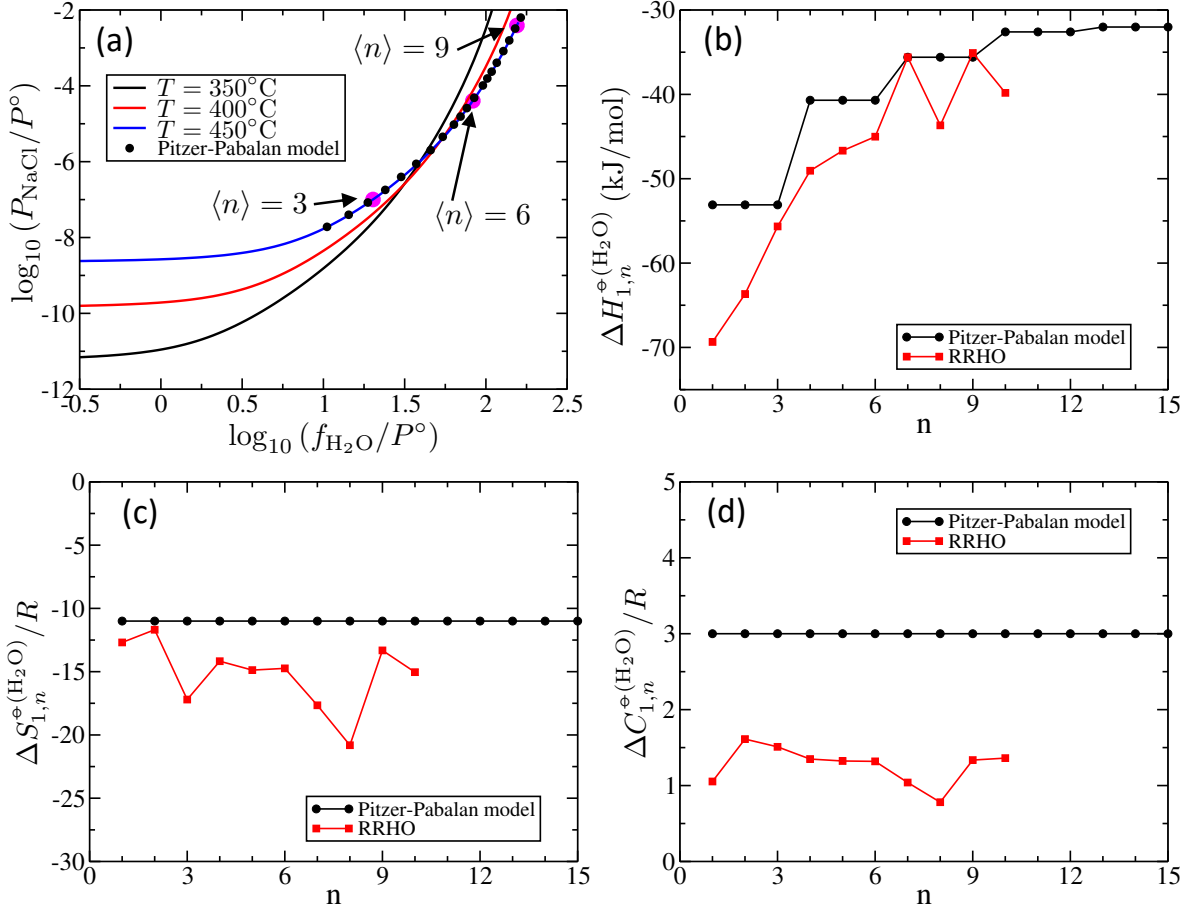


Figure 9: (a) Partial pressure of NaCl-bearing water clusters generated using the parameters from the last three columns in Table 3 (solid lines). Black dots represent the data directly digitized from Figure 2 in Ref. [4]. Thermodynamic parameters from second, third and fourth numerical columns in Table 3 are compared to the RRHO results in panels (b), (c) and (d), respectively.

dration, so  $\Delta \tilde{H}_{1,n}^{\circ}$  becomes negative for larger clusters. Mean cluster size, defined by Eq. (14), increases with fugacity, so it is expected that at high fugacities the summation in Eq. (25) is dominated by large clusters with negative  $\Delta \tilde{H}_{1,n}^{\circ}$ , thus resulting in negative  $\left(\frac{\partial P_X}{\partial T}\right)_f$  and so retrograde solubility is observed. For small clusters, however, the temperature dependence of  $P_X$  is domi-

nated by the thermodynamics of sublimation (Figure 8), and so  $P_X$  grows rapidly with temperature at low fugacities and the solubility is “normal” (i.e., not retrograde). Magenta circles in Figure 9(a) denote fugacities where  $\langle n \rangle = 3, 6, 9$  at  $T = 450^{\circ}\text{C}$ . The temperature derivative of  $P_X$  is seen to change sign at  $\langle n \rangle \sim 4-5$ . In agreement with this, comparison of data in Table 2 and Figure 9(b) implies that  $\Delta \tilde{H}_{1,n}^{\circ}$  is negative for  $n \gtrsim 5$ . As  $f \rightarrow 0$ , Eq.

(13) reduces to fugacity-independent  $P_X = P^\circ e^{-\Delta G_s^\circ/RT}$ , which is the pressure of the anhydrous salt vapor. Accordingly,  $P_{\text{NaCl}}$  becomes constant at low fugacities in Figure 9(a). One can verify that the values of  $P_{\text{NaCl}}$  at  $f \rightarrow 0$ , taken as a function of temperature, coincide with the black line in Figure 8.

As described above, we employed quantum chemistry calculations (Gaussian 16) together with the thermochemical code Magpie to calculate the thermodynamics of NaCl-bearing water clusters within the RRHO approximation. The results of these calculations, plotted by red squares in Figure 9(b)-(d), are seen to be in reasonable agreement with the Pitzer-Pabalan model. Notable deviations for the entropy and for heat capacity could be rationalized as follows. A known deficiency of the RRHO approach is that it approximates all the vibrational modes as strictly harmonic [22, 26]. However, soft vibrational modes of van der Waals-bonded clusters are expected to be rather anharmonic (e.g., internal hindered rotations), and so RRHO is expected to underestimate the change in entropy and heat capacity of a cluster upon addition of a water molecule. This is in qualitative agreement with what is observed in Figure 9(c) and (d). Another source of inaccuracy of the RRHO calculations in this work is that, as discussed above, it takes into account only a single cluster of all the clusters with the same stoichiometry - the one with the lowest energy. Not including any energetically sub-optimal clusters (i.e., via the Boltzmann distribution of all accessible configurations for the same stoichiometry) is expected to result in underestimating the enthalpy and entropy of hydration, which is again in qualitative agreement with Figure 9(c) and (d).

General considerations for the dependence of  $\Delta H_{1,n}^{\ominus(\text{H}_2\text{O})}$ ,  $\Delta S_{1,n}^{\ominus(\text{H}_2\text{O})}$  and  $\Delta C_{1,n}^{\ominus(\text{H}_2\text{O})}$  on the number of water molecules  $n$  are as follows. The enthalpy of hydration  $\Delta H_{1,n}^{\ominus(\text{H}_2\text{O})}$  has to be negative due to attractive interaction of a cluster with an added water molecule. Due to Coulomb screening of interaction with the salt molecule, this interaction is weaker for larger clusters so the magnitude of  $\Delta H_{1,n}^{\ominus(\text{H}_2\text{O})}$  decreases with  $n$ . The entropy change  $\Delta S_{1,n}^{\ominus(\text{H}_2\text{O})}$  is expected to be strongly negative since the large translational entropy of a water molecule is substituted with the much smaller vibrational one. The standard molar translational entropy of an ideal gas of water molecules at the reference temperature  $T_{\text{ref}} = 500 \text{ K}$  is evaluated using the Sackur-Tetrode equation [30] to be  $S_{0,1}^\ominus/R \approx 18.7$ . If this entropy is lost upon addition of the water molecule to a cluster and nothing else changed, the result would be  $\Delta S_{1,n}^{\ominus(\text{H}_2\text{O})}/R = -18.7$ , which is not too inconsistent with

the RRHO results in Figure 9(c). The entropy change, extracted by Pitzer and Pabalan, is not as negative, implying that the translational entropy is not completely lost but rather substituted with a lower, but still substantial, entropy of soft vibrational modes. Assuming that the three translational and three rotational degrees of freedom (DOF) of an isolated water molecule become six classical harmonic vibrational DOFs upon bonding to a cluster, the heat capacity change would be  $\Delta C_{1,n}^{\ominus(\text{H}_2\text{O})}/R = 2$ , which is comparable to what is shown in Figure 9(d).

It is important to remember that the general considerations just above only concern the general "smooth" dependence of  $\Delta H_{1,n}^{\ominus(\text{H}_2\text{O})}$ ,  $\Delta S_{1,n}^{\ominus(\text{H}_2\text{O})}$  and  $\Delta C_{1,n}^{\ominus(\text{H}_2\text{O})}$  on  $n$ . They cannot account for a specific way a water molecule forms bonds with a given cluster, and how this cluster geometry rearranges upon this hydration. It is therefore expected that some "noise", originating from the specific details of interaction of water and salt molecules within a cluster, should be present on top of the general smooth dependence on  $n$  discussed above. This "noise" is clearly seen on top of the general smooth dependence on  $n$  in the RRHO results (red lines) in Figure 9(b)-(d).

### 5.1. Fitting Procedure

The dependence of  $\Delta H_{1,n}^{\ominus(\text{H}_2\text{O})}$  on  $n$  reflects the nature of interaction of a water molecule with a  $(1, n - 1)$ -cluster. Pitzer and Pabalan used the piecewise constant functional form with all the steps of the same length of 3. This form is illustrated by black dots in Figure 9. To explore and accurately control the degree of underfitting/overfitting we need a more general and flexible functional form. We choose a continuous piecewise linear function, which if comprising  $K$  kinks, is specified by  $K$  kink positions,  $K + 1$  tangents, and one absolute value - the value of the function at  $n = 1$ . For instance, a  $K$ -kink representation of  $\Delta H_{1,n}^{\ominus(\text{H}_2\text{O})}$  as a function of  $n$  is specified by its piecewise-constant derivative

$$\frac{\partial \Delta H_{1,n}^{\ominus(\text{H}_2\text{O})}}{\partial n} = \begin{cases} h_1, & \text{if } n < n_1 \\ h_i, & \text{if } n_{i-1} \leq n < n_i \quad (i \in [2, K]), \\ h_{K+1}, & \text{if } n > n_K \end{cases} \quad (26)$$

and by the value of  $\Delta H_{1,1}^{\ominus(\text{H}_2\text{O})}$ . For example, a 0-kink representation, i.e., a simple linear dependence, is defined by two parameters ( $\Delta H_{1,1}^{\ominus(\text{H}_2\text{O})}$  and  $h_1$ ), whereas four parameters are required to define a 2-kink function ( $\Delta H_{1,1}^{\ominus(\text{H}_2\text{O})}$ ,  $h_1$ ,  $h_2$ ,  $n_1$ ). Kink positions  $n_i$  are assumed continuous numbers, which simplifies fitting by allowing their continuous variation in standard optimization routines. Similar representations could be introduced

for  $\Delta S_{1,n}^{\ominus(\text{H}_2\text{O})}$  and  $\Delta C_{1,n}^{\ominus(\text{H}_2\text{O})}$ . We find, however, that it is sufficient to represent them by a single  $n$ -independent value each.

To extract the parameters, like those in Eq. (26), from fitting, one has to define a function of these parameters that encodes the deviation of the model from the benchmark experimental results and then minimize that function. For benchmark data, similar to that in Figure 9(a) where we have  $P_X$  as a function of  $f$  at several temperatures, such deviation function is introduced as follows. We first substitute the water fugacity by a new variable

$$x = \frac{\log_{10} [f/f^{(min)}]}{\log_{10} [f^{(max)}/f^{(min)}]}, \quad (27)$$

where  $(f^{(min)}, f^{(max)})$  covers the full experimentally accessible range of fugacities. Similarly, for the partial pressure of salt-bearing water clusters we have

$$y = \frac{\log_{10} [P_X/P_X^{(min)}]}{\log_{10} [P_X^{(max)}/P_X^{(min)}]}. \quad (28)$$

Upon these substitutions, Figure 9(a) - a standard way of presenting  $P_X$  dependence on water fugacity in the literature - effectively becomes a linear-linear plot (as opposed to e.g., log-log), the abscissa and ordinate ranging from 0 to 1. Then, at fixed temperature  $T = T_i$ , the deviation of the model data for the partial pressure of salt-bearing clusters (taken as a function of fugacity  $f$ ), from the experimental results is calculated as

$$d_i = \int_{x_{i,min}}^{x_{i,max}} dx [y_i^{(mod)}(x) - y_i^{(exp)}(x)]^2, \quad (29)$$

where  $x_{i,min}$  and  $x_{i,max}$  are the minimum and maximum values of  $x$  available experimentally at temperature  $T_i$ . The integral is evaluated by interpolating  $y_i^{(mod)}$  and  $y_i^{(exp)}$  to make them continuous functions of  $x$ . The full deviation function is then evaluated by summing up all the single-temperature deviations as

$$D = \frac{1}{2} \log_{10} \left[ \frac{1}{N} \sum_{i=1}^N d_i \right], \quad (30)$$

where  $N$  is the number of temperatures. The rationale behind this definition of deviation can be illustrated by the following example. Suppose that the model results for  $\log_{10} P_X/P^\circ$  deviate by exactly 1% of  $\log_{10} [P_X^{(max)}/P_X^{(min)}]$  from the experimental data at all water fugacities. That would mean a deviation of the model curves from experimental by 1% of the vertical range in Figure 9(a), treating it as a linear-linear plot.

The deviation of this magnitude is still be rather noticeable in a figure. This deviation produces  $d_i = 10^{-4}$  and therefore  $D = -2$ . On the other hand, the deviation of the model results, represented by  $\log_{10} P_X/P^\circ$ , by 0.1% of  $\log_{10} [P_X^{(max)}/P_X^{(min)}]$  from the experimental data, results in  $D = -3$  and is perceived as a perfect agreement between theory and experiment when plotted in a figure similar to Figure 9(a). Therefore, the value of  $D$  represents the decimal logarithm of the deviation of the model  $\log_{10} P_X$  from its experimental counterpart, normalized to the entire span of  $\log_{10} P_X$  in experiment.

The minimization of the total deviation with respect to the model parameters is performed by the Broyden-Fletcher-Goldfarb-Shanno (BFGS) quasi-Newton algorithm [31], as implemented in SciPy standard Python library. This algorithm relies on the smoothness of a function to minimize, which is not the case in this work since the underlying dependence of thermodynamic parameters on the cluster size, Eq. (26), is piecewise-linear. In particular, we noticed that this non-smoothness sometimes comprises the BFGS ability to find a minimum. To remedy that, we additionally convolute the piecewise-linear function with the normalized gaussian  $(2\pi\sigma^2)^{-1/2} e^{-n^2/2\sigma^2}$ . Not too small  $\sigma$  drastically increases the robustness of the BFGS convergence. On the other hand, if  $\sigma$  is small compared to one, then the resulting function is almost the same in magnitude at all  $n$ , as the one before the convolution. We choose  $\sigma = 0.3$  in this work.

Figure 10 shows the results of fitting the data, generated from the last three columns of Table 3 (black lines), using the 0-, 1- and 2-kink function for  $\Delta H_{1,n}^{\ominus(\text{H}_2\text{O})}$ , and  $n$ -independent values for  $\Delta S_{1,n}^{\ominus(\text{H}_2\text{O})}$  and  $\Delta C_{1,n}^{\ominus(\text{H}_2\text{O})}$ . First, we perform the fitting by the 0-kink function to represent  $\Delta H_{1,n}^{\ominus(\text{H}_2\text{O})}$ . The results of this fitting are plotted by dashed red lines in panel (a). The resulting dependence of  $\Delta H_{1,n}^{\ominus(\text{H}_2\text{O})}$  on  $n$  is shown in Figure 10(b) by the solid red line. More specifically, the parameters produced by fitting are compiled in Table 4. As is seen, the fit quality is reasonable although the deviations between the solid black and dashed red lines are quite noticeable in Figure 10(a). The resulting best value of the deviation function is  $-1.901$ .

The results of fitting for the 1-kink enthalpy function are shown by blue circles in Figure 10(a). As is seen, the agreement with the data generated from the Pitzer-Pabalan model is very good, as is also clear from the best value of the deviation function:  $-2.905$ . This significant improvement of the fitting quality when switching from the 0-kink to 1-kink representation for  $\Delta H_{1,n}^{\ominus(\text{H}_2\text{O})}$  suggests that the 0-kink model results in un-



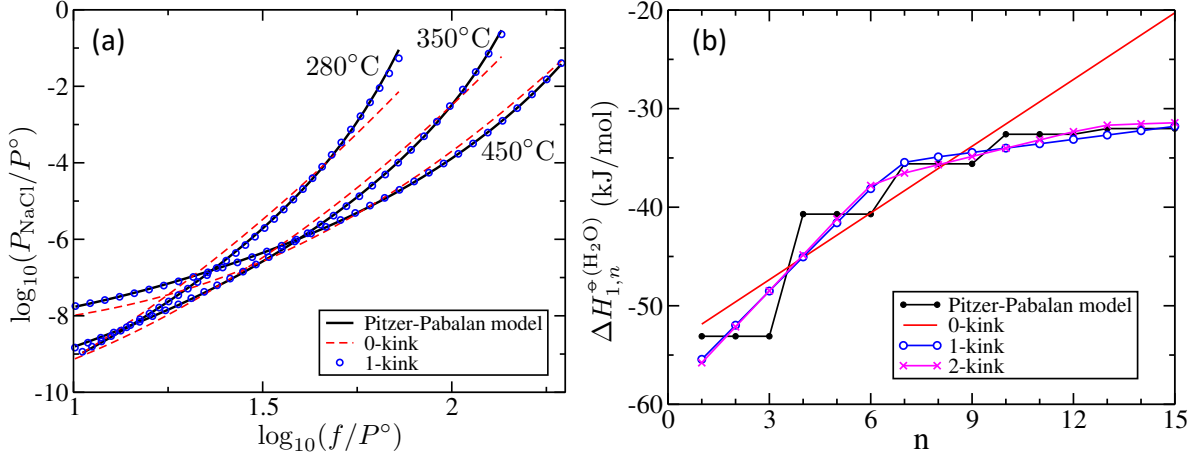


Figure 10: Fitting of the partial pressure of the ideal gas of  $\text{NaCl}:(\text{H}_2\text{O})_n$  clusters, generated from the last three columns in Table 3 at three different temperatures (280°C, 350°C and 450°C). Fitting is performed using the continuous piecewise linear representation of  $\Delta H_{1,n}^e(\text{H}_2\text{O})$  as a function of  $n$ , whereas entropy and heat capacity of hydration are taken  $n$ -independent. The dependence of partial pressure of NaCl-bearing water clusters on the water fugacity for the Pitzer-Pabalan model (black lines) and resulting fitting with the few-kink model (dashed red lines, blue circles) are given in panel (a). Enthalpy of hydration for the Pitzer-Pabalan model (black line) and the few-kink models (red, blue, magenta lines) are plotted in panel (b).

$\Delta S_{1,n}^e(\text{H}_2\text{O})/R$	$\Delta C_{1,n}^e(\text{H}_2\text{O})/R$	$\Delta H_{1,1}^e(\text{H}_2\text{O})$ (kJ/mol)	$h_1$ (kJ/mol)
-10.85	2.744	-51.86	2.256

Table 4: The results for fitting NaCl solubility with the 0-kink representation of  $\Delta H_{1,n}^e(\text{H}_2\text{O})$ .

derfitting. The resulting dependence of  $\Delta H_{1,n}^e(\text{H}_2\text{O})$  on  $n$  is plotted as blue circles in panel (b). The resulting parameters are given in Table 5. We observed that if we do not allow  $\Delta C_{1,n}^e(\text{H}_2\text{O})/R$  to vary and set it to be an arbitrary constant value within interval from 2 to 4, it changes the value of the deviation function by  $\approx 0.05$  at most. This means that, similarly to what we observed when fitting the thermodynamics of sublimation, Table 2,  $\Delta C_{1,n}^e(\text{H}_2\text{O})$  cannot be reliably extracted from the fitting. Equilibrium constants  $K_n = e^{-\Delta \hat{G}_{1,n}^\circ/RT}$ , where  $\Delta \hat{G}_{1,n}^\circ(T)$  is evaluated using the parameters in Table 5 and the first numerical column in Table 2, are tabulated in Table A.9 for a range of  $n$  and  $T$ .

Finally, we perform the fitting using the 2-kink function for enthalpy. The result of this fitting is not shown in Figure 10(a) since it superimposes with the 1-kink results. According to the discussion just above, the heat capacity is not varied and set to  $\Delta C_{1,n}^e(\text{H}_2\text{O})/R = 3$ . The best value of the deviation function reaches  $-3.301$  in this case. The enthalpy change is shown in panel (b) by magenta crosses. It is seen that it closely follows the 1-kink enthalpy dependence at low  $n$  but then deviates slightly. The resulting parameters are given in Table 6. For the 1-kink representation for  $\Delta H_{1,n}^e(\text{H}_2\text{O})$ , where only

4 independent parameters are used, the agreement between model calculations and the benchmark is almost perfect. Introduction of the second kink does not visibly improve the quality of fit, implying that fitting with the 2-kink function to represent  $\Delta H_{1,1}^e(\text{H}_2\text{O})$  constitutes an overfitting. The original Pitzer-Pabalan  $\Delta H_{1,n}^e(\text{H}_2\text{O})$  dependence on  $n$  is defined by 5 independent parameters, as is clear from Table 3. We thus conclude that the original work represents a case of overfitting.

Finally, we want to compare our results to those obtained from a different model describing the NaCl solubility in water vapor. Figure 11 shows the dependence of NaCl weight percentage (wt%) in water vapor as a function of vapor pressure at three different temperatures. Solid lines are obtained from Eq. (12) using parameters from Table 5. Dashed lines are obtained for the vapor-solid equilibrium (liquid phase is absent) from the SoWat computer code that implements the model to analyze the properties of fluids and vapor in the  $\text{H}_2\text{O}$ -NaCl system [32–34]. As is seen, the agreement is satisfactory at higher temperatures, where, importantly, our model involves extrapolation since it was calibrated using the data only in the temperature range from 280°C to 450°C, as is seen in Figure 10(a). At lower tempera-

$\Delta S_{1,n}^{\circ(\text{H}_2\text{O})}/R$	$\Delta C_{1,n}^{\circ(\text{H}_2\text{O})}/R$	$\Delta H_{1,1}^{\circ(\text{H}_2\text{O})}$ (kJ/mol)	$h_1$ (kJ/mol)	$n_1$	$h_2$ (kJ/mol)
-10.98	3.005	-55.43	3.463	5.777	0.442

Table 5: The results for fitting NaCl solubility with the 1-kink representation of  $\Delta H_{1,n}^{\circ(\text{H}_2\text{O})}$ .

$\Delta S_{1,n}^{\circ(\text{H}_2\text{O})}/R$	$\Delta C_{1,n}^{\circ(\text{H}_2\text{O})}/R$	$\Delta H_{1,1}^{\circ(\text{H}_2\text{O})}$ (kJ/mol)	$h_1$ (kJ/mol)	$n_1$	$h_2$ (kJ/mol)	$n_2$	$h_3$ (kJ/mol)
-11.0	3 (forced)	-55.78	3.648	5.064	0.838	11.802	0.107

Table 6: The results for fitting NaCl solubility with the 2-kink representation of  $\Delta H_{1,n}^{\circ(\text{H}_2\text{O})}$ .

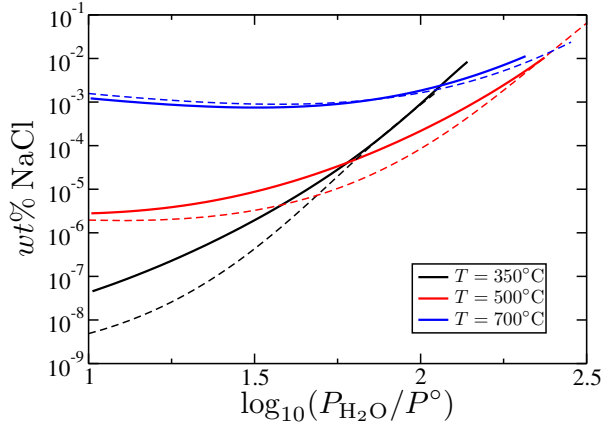


Figure 11: NaCl wt% (percentage by weight) versus water vapor pressure for three different temperatures. Solid lines are fitting results obtained in this work, Table 5. Dashed lines represent the results obtained from the the SoWat model [32, 33].

tures, the SoWat model underestimates binding of water molecules to NaCl for smaller cluster sizes.

## 6. Solubility of Copper Chloride in Water Vapor

The results of the fitting of the experimental  $P_{\text{CuCl}}$  dependence on water fugacity  $f$  for five different temperatures is plotted in Figure 12. The black circles are the experimental data from Refs. [6, 10]. To investigate the degree of underfitting/overfitting we started, as before, by fitting the experimental data with the 0-kink function for  $\Delta H_{1,n}^{\circ(\text{H}_2\text{O})}$ , taking the thermodynamics of sublimation from the third numerical column of Table 2. Entropy of hydration  $\Delta S_{1,n}^{\circ(\text{H}_2\text{O})}$  is assumed independent of  $n$ , and its value is varied in fitting. The heat capacity of hydration is not varied and set to  $\Delta C_{1,n}^{\circ(\text{H}_2\text{O})}/R = 3$ . The resulting model  $P_{\text{CuCl}}(f)$  is plotted in Figure 12 by the solid black lines. The resulting 0-kink function for  $\Delta H_{1,n}^{\circ(\text{H}_2\text{O})}$  is plotted in Figure 13(a) by the black line. The enthalpy change in the first hydration step, entropy and heat capacity changes in any hydration step, as well

as the resulting best value of the total deviation, Eq. (30), are given in the first numerical column of Table 7.

We now re-run the fitting, with the only modification to the model being the 1-kink, instead of 0-kink, function for the dependence of  $\Delta H_{1,n}^{\circ(\text{H}_2\text{O})}$  on  $n$ . The resulting thermodynamic parameters, as well as the deviation, are plotted as the thick red line in Figure 13(a) and given in the second numerical column of Table 7. The complete set of parameters extracted from the 1-kink fitting is given in Table 8. The corresponding equilibrium constants  $K_n = e^{-\Delta\tilde{G}_{1,n}^{\circ}/RT}$ , where  $\Delta\tilde{G}_{1,n}^{\circ}(T)$  is evaluated using the parameters in Table 8 and the third numerical column in Table 2, are tabulated in Table A.10 for a range of  $n$  and  $T$ . The resulting model  $P_{\text{CuCl}}(f)$  is plotted by the red lines in Figure 12. Comparing these red lines with the 0-kink results (black lines) reveals much better agreement with the experimental data at low water fugacities. This visibly better agreement is also reflected quantitatively in lower total deviation  $D$  in Table 7. Therefore, similarly to what we had for NaCl, the 0-kink model results in underfitting. Switching to the 2-kink representation for  $\Delta H_{1,n}^{\circ(\text{H}_2\text{O})}$  does not improve the total deviation for the assumed number of significant digits, as is seen in the third numerical column of Table 7. The resultant model curves for  $P_{\text{CuCl}}(f)$  in the 2-kink case are not plotted in Figure 12, since they would practically coincide with those generated in the 1-kink case. Comparing the thick red and dashed blue lines in Figure 13 we see that all the 2-kink fitting improvement is only a marginal smoothing of the  $\Delta H_{1,n}^{\circ(\text{H}_2\text{O})}$  dependence on  $n$  at  $n \sim 2$ . Therefore, we conclude that the temperature range and scattering in the adopted experimental data for CuCl allows one to extract more accurate dependence of  $\Delta H_{1,n}^{\circ(\text{H}_2\text{O})}$  on  $n$  than that encoded by a 0-kink function. On the other hand, assuming the 2-kink model results in an overfit. This is the reason why only the parameters for the 1-kink representation of the hydration enthalpy of CuCl are explicitly given in this work, Table 7.



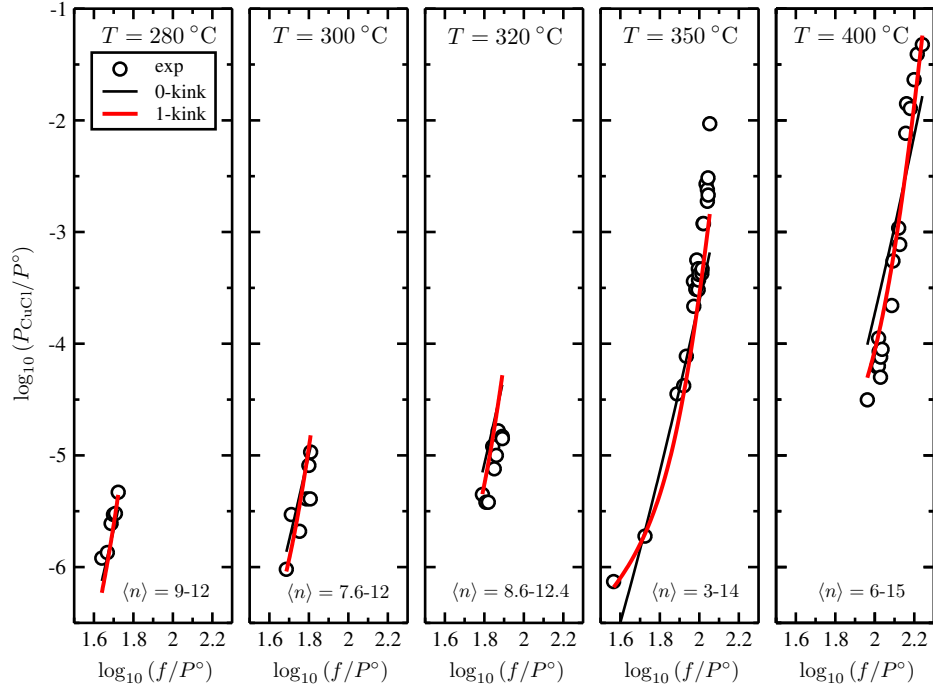


Figure 12: Partial pressure of CuCl-bearing water clusters versus the water fugacity for five different temperatures. Experimental data from Ref. [10] is depicted by black circles. Fitting results are plotted by the black and red lines for the 0- and 1-kink models of  $\Delta H_{1,n}^{\ominus(\text{H}_2\text{O})}$ , respectively.

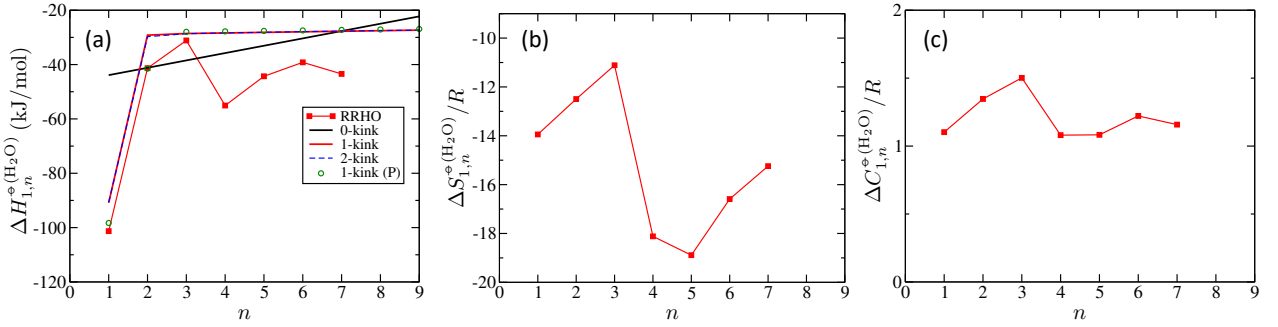


Figure 13: (a) Standard molar enthalpy of hydration of CuCl-bearing clusters. Solid black, solid red and dashed blue lines correspond to the first three numerical columns in Table 7. Green circles correspond to the last column in Table 7. Standard molar entropy and heat capacity of hydration are presented in panels (b) and (c), respectively. Red squares in all the panels correspond to the results of the RRHO calculations.

	0-kink	1-kink	2-kink	1-kink	1-kink (P)
$\Delta H_{1,1}^{\ominus(\text{CuCl})}$ (kJ/mol)	-43.90	-89.43	-90.31	-86.54	-98.30
$\Delta S_{1,n}^{\ominus(\text{CuCl})}/R$	-9.198	-9.719	-9.732	-9.331	-9.684
$\Delta C_{1,n}^{\ominus(\text{CuCl})}/R$	3	3	3	1	3
$D$	-1.808	-1.995	-1.995	-2.001	-1.998

Table 7: Results for the CuCl solubility fitting. The fourth numerical column shows fitting results where the heat capacity change was set to  $\Delta C_{1,n}^{\ominus(\text{H}_2\text{O})}/R = 1$  instead of usual  $\Delta C_{1,n}^{\ominus(\text{H}_2\text{O})}/R = 3$  (the first three numerical columns). The last column shows the fitting results where the enthalpy of hydration was represented by the same 1-kink form, but the sublimation data was taken from Pankratz (the fourth numerical column in Table 2) and not from JANAF (the third numerical column) thermochemical tables.

$\Delta S_{1,n}^{\circ(\text{H}_2\text{O})}/R$	$\Delta C_{1,n}^{\circ(\text{H}_2\text{O})}/R$	$\Delta H_{1,1}^{\circ(\text{H}_2\text{O})}$ (kJ/mol)	$h_1$ (kJ/mol)	$n_1$	$h_2$ (kJ/mol)
-9.714	3 (forced)	-86.78	60.86	0.9575	0.1915

Table 8: The results of the fitting CuCl solubility with the 1-kink representation of  $\Delta H_{1,n}^{\circ(\text{H}_2\text{O})}$ .

Up to this point, we have used the fixed value of the heat capacity of hydration set to  $\Delta C_{1,n}^{\circ(\text{H}_2\text{O})}/R = 3$ . To explore the sensitivity of the fitting quality on the value of this parameter, we also perform a 1-kink fitting with the heat capacity set to  $\Delta C_{1,n}^{\circ(\text{H}_2\text{O})}/R = 1$ . The resulting hydration parameters and total deviation are given in the fourth numerical column of Table 7. As is seen, the total deviation changes only marginally, and the model  $P_{\text{CuCl}}(f)$  curve, if plotted in Figure 12, would practically coincide with those for the 1-kink case discussed before. Therefore,  $\Delta C_{1,n}^{\circ(\text{H}_2\text{O})}$  can not be reliably extracted from the adopted experimental data. We choose to set the heat capacity of hydration to  $\Delta C_{1,n}^{\circ(\text{H}_2\text{O})}/R = 3$  for definiteness.

There is a spread in CuCl sublimation parameters in the literature, illustrated in this work by the difference between the JANAF and Pankratz data, the third and fourth numerical columns in Table 2. Re-fitting the experimental data assuming Pankratz data for CuCl sublimation results in a 1-kink dependence of  $\Delta H_{1,n}^{\circ(\text{H}_2\text{O})}$  on  $n$  shown by the green circles in Figure 13, and the fifth numerical column in Table 7. We see that the fit effectively compensates the increase of the sublimation enthalpy, when going from JANAF to Pankratz sublimation data, by the respective decrease of the enthalpy of hydration when forming CuCl:H<sub>2</sub>O. This compensation is possible because what enters Eq. (13) is not the sublimation or hydration parameters separately, but only through  $\Delta \tilde{G}_{1,n}^{\circ} = \Delta G_s^{\circ} + \Delta G_{1,1}^{\circ(\text{H}_2\text{O})} + \Delta G_{1,2}^{\circ(\text{H}_2\text{O})} + \dots + \Delta G_{1,n}^{\circ(\text{H}_2\text{O})}$ . Accordingly, if the experimental data does not extend to very low water fugacities where the contribution of anhydrous CuCl monomers to  $P_{\text{CuCl}}$  is dominant, fitting the experimental data with Eq. (13) can not provide, for example,  $\Delta H_s^{\circ}$  and  $\Delta H_{1,1}^{\circ(\text{H}_2\text{O})}$  separately. Evaluating Eq. (14) in the context of the red curves in Figure 12, one can find that the lowest mean cluster size is around  $\langle n \rangle \approx 2.3$ , achieved at the lowest fugacity at  $T = 350^\circ\text{C}$ . In particular, this means that clusters smaller than CuCl:(H<sub>2</sub>O)<sub>2</sub> do not contribute significantly to the partial pressure of the salt-bearing water clusters in the adopted experimental data, so no fitting is able to separately provide  $\Delta H_s^{\circ}$ ,  $\Delta H_{1,1}^{\circ(\text{H}_2\text{O})}$  and  $\Delta H_{1,2}^{\circ(\text{H}_2\text{O})}$ . This is precisely why we use the thermochemical tables that provide  $\Delta G_s^{\circ}$  independently.

Results for our RRHO calculations for enthalpy, en-

trophy and heat capacity of hydration, calculated at  $T_{\text{ref}}$ , are plotted by red squares in Figure 13. Similar to the NaCl case, RRHO systematically underestimates the enthalpy and entropy of hydration, compared to those obtained from fitting, if the clusters are not too small. We expect that this is at least partially due to accounting for only a single lowest-energy cluster of a given stoichiometry (1,  $n$ ). In principle, Eq. (2b) can be used with the understanding that the both initial and final clusters are each in fact thermodynamic ensembles of clusters of different configurations but the same stoichiometry. Each such ensemble has larger enthalpy and larger entropy than the lowest-energy cluster from this ensemble. The difference between the thermodynamic ensemble and the lowest-energy cluster from this ensemble should be the least pronounced for smaller clusters, where the significant energy separation between the lowest and next-to-lowest configurations may prevent the latter from contributing significantly to each (1,  $n$ ) ensemble. In other words, the smaller the cluster, the better the corresponding thermodynamic ensemble is represented by the lowest-energy cluster from this ensemble. We therefore expect that the net result of accounting only for the lowest-energy cluster in Eq. (2b) is the underestimation of enthalpy and entropy of hydration at high fugacities. In particular, since we take only the lowest-energy cluster and not the ensemble of clusters of the same stoichiometry we underestimate the enthalpy of the initial and final cluster in Eq. (2b). Not accounting for all the clusters of a given stoichiometry underestimates the entropy.

To this point, fitting was performed while constraining the sublimation parameters to those extracted from the thermochemical tables. This is not always possible for other materials due to the lack of reliable thermochemical data. To demonstrate what happens if sublimation parameters are not available, CuCl experimental data (circles in Figure 12) was fit assuming  $\Delta H_s^{\circ}$  and  $\Delta S_s^{\circ}$  are unconstrained. Heat capacity of sublimation is still taken as constrained since, as we saw above, heat capacities are related to weak second-order deviations of Gibbs free energy with respect to temperature and, as such, are not recovered reliably from fitting. Again, we set the heat capacity of sublimation to  $\Delta C_s^{\circ}/R = -3$  - a typical value for sublimation, as can be seen from

Table 2. The results of such fitting, presented as the enthalpy  $\Delta\tilde{H}_{1,n}^\circ$  and Gibbs free energy  $\Delta\tilde{G}_{1,n}^\circ$  of formation of a  $(1,n)$ -cluster formed out of  $n$  gaseous water molecules and a single CuCl monomer extracted from the crystalline bulk, are plotted in Figure 14 as the thin black and blue lines, respectively. Multiple black and

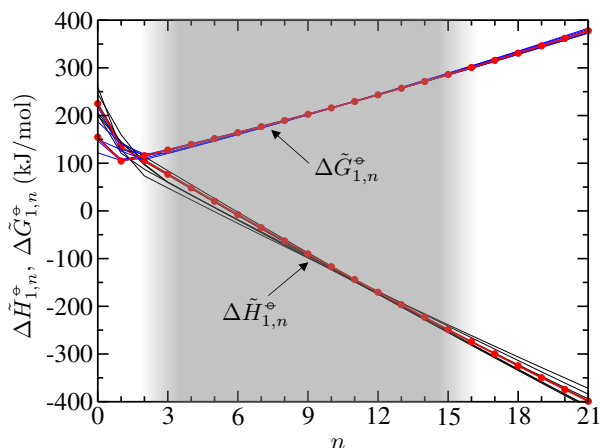


Figure 14: The change of the standard molar enthalpy and Gibbs free energy for the process  $\text{CuCl}(\text{cr}) + n\text{H}_2\text{O} \rightarrow \text{CuCl}:(\text{H}_2\text{O})_n$  at  $T = T_{\text{ref}}$ . The black and blue lines are obtained by allowing  $\Delta H_s^\circ$  and  $\Delta S_s^\circ$  to vary when fitting. The red dots represent the results of the previous 1-kink fitting, Figure 13(a), where the sublimation parameters were not varied and set to the values in the third numerical column of Table 2.

blue lines are obtained by varying initial values of the fitting parameters and then performing BFGS optimization. Values of the deviation function in the range from  $-1.99$  to  $-2.01$  are reached for all the plotted black lines and the resulting  $P_{\text{CuCl}}(f)$  lays on top of the red lines in Figure 12. It is seen that the black (or blue) lines, corresponding to different initial values of fitting parameters fed to BFGS before starting the minimization, do not coincide. They also do not coincide with the red dots, which represent the previous 1-kink fitting results where the sublimation parameters were not varied and taken from the third numerical column of Table 2. This means that the available experimental data is not sufficient to uniquely constrain the newly introduced fitting parameters, i.e., those of sublimation. In particular, since  $\Delta\tilde{H}_{1,0}^\circ = \Delta H_s^\circ$ , we see that the extracted enthalpy of sublimation varies in the range from 200 to 260 kJ/mol. Slopes of extracted  $\Delta\tilde{H}_{1,n}^\circ$  are also varying suggesting that because of the uncertainty in  $\Delta H_s^\circ$ , the enthalpies of hydration  $\Delta\tilde{H}_{1,n}^{\circ(\text{H}_2\text{O})}$  can not be uniquely recovered.

Fitting the experimental data with Eq. (13) allows one to evaluate the mean cluster size as a function of  $f$

using Eq. (14). Ranges of the mean cluster size, corresponding to the red lines in Figure 12, are given in each panel of that figure. As is seen, clusters of sizes smaller than 3 or large than 15 are inaccessible in the experiment. The gray shading in Figure 14 highlights this range. Since the fitting is performed with Eq. (13), and of all the thermodynamic potentials it is  $\Delta\tilde{G}_{1,n}^\circ$  that enters this expression directly, we expect the extracted values of  $\Delta\tilde{G}_{1,n}^\circ$  in the range  $3 \lesssim n \lesssim 15$  to be most reliable. This is indeed the case in Figure 14, where blue lines practically superimpose within the gray shading area. The reliability of the extracted temperature dependence of  $\Delta\tilde{G}_{1,n}^\circ$ , expressed by values of  $\Delta\tilde{H}_{1,n}^\circ$ ,  $\Delta\tilde{S}_{1,n}^\circ$  and  $\Delta\tilde{C}_{1,n}^\circ$ , is expected to grow when the experimentally accessible temperature range increases. The spread in  $\Delta\tilde{H}_{1,n}^\circ$  is seen to be larger than that of  $\Delta\tilde{G}_{1,n}^\circ$  in Figure 14 since the former does not enter Eq. (13). However,  $\Delta\tilde{H}_{1,n}^\circ$  still becomes relatively well defined, i.e., the spread is minimized, in the middle of the  $3 \lesssim n \lesssim 15$  range signifying that  $\frac{\partial(\Delta\tilde{G}_{1,n}^\circ)}{\partial T} = -\Delta\tilde{S}_{1,n}^\circ = (\Delta\tilde{G}_{1,n}^\circ - \Delta\tilde{H}_{1,n}^\circ)/T$  is extracted relatively reliably. The reliability of extraction of the magnitude and temperature dependence of  $\Delta\tilde{G}_{1,n}^\circ$  from fitting is thus directly related to, respectively, the range of experimentally accessible water fugacities and temperatures.

## 7. Discussion

In this section, we first discuss the chemical nature and strength of bonding in the  $\text{NaCl}:\text{H}_2\text{O}$  and  $\text{CuCl}:\text{H}_2\text{O}$  clusters. Then, in Sec. 7.3, the large-cluster asymptotic behavior of the enthalpy of hydration is investigated. Finally, the assumption of temperature-independent heat capacity change  $\Delta C^\circ$  is justified in Sec. 7.4.

### 7.1. Nature of chemical bonding in $\text{X}:\text{H}_2\text{O}$

Figure 15 shows the dependence of the enthalpy of hydration on cluster size, where the enthalpies of hydration for NaCl (black circles) and CuCl (red diamonds) are reproduced from Figures 10(b) and 13(a), respectively. As is seen, the dependence of  $\Delta H_{1,n}^{\circ(\text{H}_2\text{O})}$  on  $n$  is qualitatively different for these two salts: (i) the enthalpy of the first hydration  $\Delta H_{1,1}^{\circ(\text{H}_2\text{O})}$  is significantly higher in magnitude for CuCl than for NaCl, and (ii) the dependence of  $\Delta H_{1,n}^{\circ(\text{H}_2\text{O})}$  on  $n$  is smoother for NaCl. We believe that these substantial differences arise from the chemically different nature of interaction of a water molecule with a salt monomer. The configurations of  $\text{NaCl}:\text{H}_2\text{O}$  and  $\text{CuCl}:\text{H}_2\text{O}$  clusters, as obtained from quantum chemical calculations, are drawn in Figures

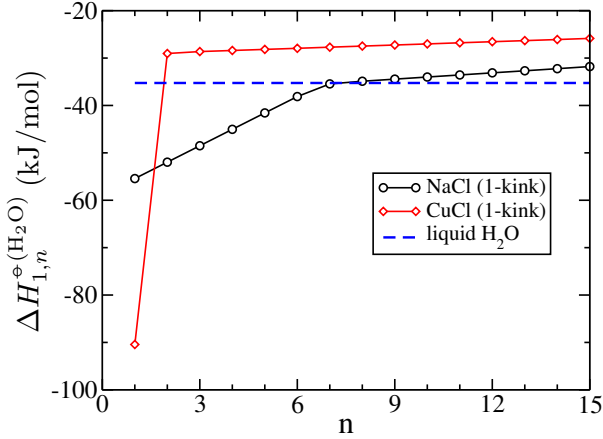


Figure 15: Enthalpy of hydration of  $\text{NaCl}:(\text{H}_2\text{O})_n$  clusters (black circles) and  $\text{CuCl}:(\text{H}_2\text{O})_n$  clusters (red diamonds), replotted from Figures 10(b) and 13(a), respectively. The dashed blue line is  $\Delta H_{0,\infty}^{\circ(\text{H}_2\text{O})}$  from Table 1.

2(c) and (d), respectively. The interaction of the water molecule with the NaCl monomer is seen to result in a cluster where the oxygen is attracted to Na, and hydrogen to Cl, resulting in a typical dipole-dipole complex. On the other hand, oxygen binds to Cu in the copper chloride monomer via the coordinate covalent bond where the lone electron pair of oxygen is donated to the empty electronic orbital of the copper. This covalent bonding results in a linear configuration of the  $\text{CuCl}:\text{H}_2\text{O}$  cluster and the significantly larger magnitude of the enthalpy of first hydration, compared to that for sodium chloride. The observed linear configuration is consistent with previous observations [35, 36].

The first hydration of an anhydrous CuCl molecule saturates the electron configuration of copper, so all the subsequent hydration steps, just like all the hydration steps of NaCl, proceed through the dipole-dipole bonding of water molecules to a cluster. Our quantum chemical calculations with the Gaussian 16 software package yield the dipole moments of 9.0 D, 5.1 D and 2.2 D for the isolated sodium chloride, copper chloride and water molecules, respectively. This means that the strength of dipole-dipole bonding is expected to be larger for the NaCl-based complexes than for CuCl-based ones. This is the reason why the magnitude of  $\Delta H_{1,n}^{\circ(\text{H}_2\text{O})}$  is noticeably higher for the sodium chloride than for copper chloride at  $n \geq 2$ . This difference is also reflected in the lowest-energy geometries of the  $\text{X}:(\text{H}_2\text{O})_2$  clusters in Figure 2, where the second water molecule binds directly to the salt molecule in panel (c), whereas the water-water hydrogen bond is formed in panel (d).

## 7.2. Strength of the dipole-dipole interaction in $\text{NaCl}:\text{H}_2\text{O}$

Here, we explore whether the value of the enthalpy of hydration  $\Delta H_{1,1}^{\circ(\text{H}_2\text{O})}$  for NaCl, obtained from the fitting, is physically reasonable. In Sections 3 and 4 we evaluated the thermodynamics of formation of  $\text{H}_2\text{O}$  and NaCl dimers, respectively. Since both of those dimers are bound by the dipole-dipole interaction this information can be used to estimate the enthalpy of formation of the  $\text{NaCl}:\text{H}_2\text{O}$  cluster, which is also bound by the dipole-dipole interaction. The change of molar internal energy upon the formation of a dipole-dipole bond between species A and B is approximately [37]

$$\Delta E_{AB} = E_{AB} - E_A - E_B = -C \frac{d_A d_B}{r_{AB}^3}, \quad (31)$$

where  $d_A$ ,  $d_B$  are the electric dipole moments of the species, and  $r_{AB}$  is the characteristic distance between them in the AB cluster. The constant prefactor  $C$  will cancel out from the final expression for the enthalpy. The molar enthalpy of the ideal gas is  $H^\circ = E^\circ + RT_{\text{ref}}$  and, therefore, we have

$$\Delta H_{AB}^\circ = H_{AB}^\circ - H_A^\circ - H_B^\circ = -C \frac{d_A d_B}{r_{AB}^3} - RT_{\text{ref}}. \quad (32)$$

This equation is inverted to obtain the characteristic distance between the two molecules in a dimer

$$r_{AB} = \left[ -\frac{\Delta H_{AB}^\circ + RT_{\text{ref}}}{C d_A d_B} \right]^{-1/3}. \quad (33)$$

Using this approach, we express  $r_{(\text{H}_2\text{O})_2}$  and  $r_{(\text{NaCl})_2}$  as functions of  $\Delta H_{0,2}^{\circ(\text{H}_2\text{O})}$  and  $\Delta H_{2,0}^{\circ(\text{NaCl})}$ , respectively, and then estimate the characteristic distance between the molecules in the  $\text{NaCl}:\text{H}_2\text{O}$  cluster as a simple average of the inter-molecular distances in the two homogeneous dimers, i.e.,  $r_{\text{NaCl}:\text{H}_2\text{O}} = (r_{(\text{NaCl})_2} + r_{(\text{H}_2\text{O})_2})/2$ . The enthalpy of formation of the  $\text{NaCl}:\text{H}_2\text{O}$  cluster is then

$$\Delta H_{1,1}^{\circ(\text{H}_2\text{O})} = -C \frac{d_{\text{NaCl}} d_{\text{H}_2\text{O}}}{r_{\text{NaCl}:\text{H}_2\text{O}}^3} - RT_{\text{ref}}. \quad (34)$$

The constant prefactor  $C$  cancels out and, by taking  $\Delta H_{0,2}^{\circ(\text{H}_2\text{O})} = -16.59 \text{ kJ/mol}$  from Table 1 and  $\Delta H_{2,0}^{\circ(\text{NaCl})} \approx -200 \text{ kJ/mol}$  from Figure 6(a), we obtain  $\Delta H_{1,1}^{\circ(\text{H}_2\text{O})} = -53.5 \text{ kJ/mol}$ , which is very close to the value of  $-55.43 \text{ kJ/mol}$  obtained from the fitting and reported in Table 5. We thus see the value obtained in the fitting is reasonable on the grounds of simple crude estimates based on the physics of the dipole-dipole interaction.

### 7.3. Large- $n$ behavior of the enthalpy of hydration

The thermodynamics of hydration of a very large cluster  $X:(H_2O)_n$  is not expected to be sensitive to the presence of the monomer  $X$  within it. More accurately, we approximate a large  $(1, n)$ -cluster as a droplet of continuous dielectric liquid with a point dipole at its center, representing  $X$ . The optimal shape of the droplet is generally non-spherical and determined by the interplay between the surface tension and the magnitude of the dipole, the latter favoring non-sphericity through the Keesom interaction [30]. However, the surface tension dominates for the sufficiently large droplets resulting in a spherical shape [38]. Molar internal energy of an ideal gas of such droplets can be approximated as [20]

$$E_{1,n}^\circ \approx E_{\text{liq}}n + \sigma n^{2/3}, \quad (35)$$

where  $E_{\text{liq}}$  is the internal energy corresponding to a mole of water molecules residing in the bulk liquid water and  $\sigma > 0$  represents the positive surface energy of the droplet ( $n^{2/3}$  is proportional to the droplet surface area). The corresponding enthalpy is  $H_{1,n}^\circ = E_{1,n}^\circ + RT_{\text{ref}}$  and so the standard enthalpy of hydration of the large clusters is

$$\begin{aligned} \Delta H_{1,n}^{\circ(\text{H}_2\text{O})} &= H_{1,n}^\circ - H_{1,n-1}^\circ - H_{0,1}^\circ \\ &\approx E_{\text{liq}} - H_{0,1}^\circ + \frac{2}{3}\sigma/n^{1/3}. \end{aligned} \quad (36)$$

One has  $\Delta H_{1,\infty}^{\circ(\text{H}_2\text{O})} = E_{\text{liq}} - H_{0,1}^\circ$  and so

$$\Delta H_{1,n}^{\circ(\text{H}_2\text{O})} = \Delta H_{1,\infty}^{\circ(\text{H}_2\text{O})} + \frac{2}{3}\sigma/n^{1/3}. \quad (37)$$

An important observation here is that, since  $\sigma > 0$ ,  $\Delta H_{1,n}^{\circ(\text{H}_2\text{O})}$  has to converge to  $\Delta H_{1,\infty}^{\circ(\text{H}_2\text{O})}$  from above at large cluster sizes. However, when the clusters are small  $\Delta H_{1,n}^{\circ(\text{H}_2\text{O})} < \Delta H_{1,\infty}^{\circ(\text{H}_2\text{O})}$ . It is thus expected that when the cluster size grows starting from  $n = 1$ ,  $\Delta H_{1,n}^{\circ(\text{H}_2\text{O})}$  first grows and overshoots  $\Delta H_{1,\infty}^{\circ(\text{H}_2\text{O})}$  and then decays towards  $\Delta H_{1,\infty}^{\circ(\text{H}_2\text{O})}$  resulting in a non-monotonic behavior with respect to  $n$ . It is thus not surprising that the fitting results in Figure 15 overshoot the expected  $n \rightarrow \infty$  asymptotics plotted by the dashed blue line.

### 7.4. Magnitude and temperature dependence of $\Delta C^\circ$

The model, developed in this work, allows one to fit the experimental dependence of  $P_X$  on the water fugacity  $f$  and temperature with Eq. (13). The thermodynamics of formation of  $(1, n)$ -clusters enters this expression only through  $\Delta \tilde{G}_{1,n}^\circ$ . The temperature dependence of this

Gibbs free energy change can be written as a Taylor series with respect to  $T - T_{\text{ref}}$ . In particular, the magnitudes of the second- and third-order terms are determined by the change in heat capacity  $\Delta \tilde{C}_{1,n}^\circ$  and its temperature derivative, respectively, evaluated at  $T = T_{\text{ref}}$ . These two terms only weakly (especially the latter) affect the temperature variation of  $\Delta \tilde{G}_{1,n}^\circ$ , and, therefore, of  $P_X$ , if the range of temperature variation is not too wide. Under these conditions, it is impossible to reliably extract the change in heat capacity and its temperature derivative from fitting. Exactly that was seen in Sec. 4.1, where fitting of the sublimation data for CuCl did not allow for reliable extraction of  $\Delta \tilde{C}_s^\circ$ . Similarly, fitting the NaCl solubility with the 1-kink model in Sec. 5.1 only constrained the magnitude of  $\Delta C_{1,n}^{\circ(\text{H}_2\text{O})}$  to within a factor of  $\sim 2$ . Since even the magnitude of  $\Delta C^\circ$  is hard to extract reliably, the task of extracting its temperature derivative is unrealistic. We therefore assume that the temperature derivative is zero, which yields Eq. (15). This assumption is further supported by the observation that the heat capacities do not vary too much within the experimentally relevant temperature range in Figures 4 and 7. Furthermore, since sublimation is the reverse of adding a salt monomer to a large pure-salt cluster, i.e.,  $\Delta G_s^\circ(T) = -\Delta G_{\infty,0}^\circ(T)$ , the temperature dependence of sublimation thermodynamics is effectively represented by the blue lines in Figure 6. Specifically, it is seen in Figure 6(c) that  $\Delta C_{\infty,0}^\circ$  and therefore  $\Delta C_s^\circ$ , is a slowly varying function of temperature.

## 8. Conclusion

In this work we have developed a rigorous procedure for fitting experimental data for solubility of salts in water vapor. The procedure is based on the semi-empirical Pitzer-Pabalan model [4] and allows for extraction of thermodynamic parameters of formation of salt-bearing water clusters. As an example, we applied the procedure to the solubility of NaCl and CuCl in water vapor, obtained elsewhere [4, 10]. Reliability of the fitting was determined by controlling the degree of underfitting/overfitting. The extracted thermodynamic parameters are physically reasonable and, in particular, provide insight into the nature of bonding between anhydrous monomers of NaCl or CuCl and a single water molecule. More specifically, the magnitude of the enthalpy for this first hydration step was found to be significantly larger for CuCl than for NaCl, which was rationalized by the formation of the coordinate covalent bond in the former case and dipole-dipole bond in the latter case. This has been confirmed by the quantum

chemical computations. We believe that this methodology can now be applied to analyze the data for solubility of solid salts in water vapor for many other materials. In addition to solubility of solids in low-density water (i.e., vapor), the methods described here can also be applied to develop more comprehensive equations of state describing both phase equilibrium and volumetric (P-V-T) properties of water-salt systems [39].

In this work, we focused on the so-called “two-phase equilibrium” where the vapor of water and salt molecules was in equilibrium with the crystalline salt in the absence of the liquid phase. The resulting thermodynamic parameters can now be used to evaluate the solubility of crystalline salt in water vapor at arbitrary temperature and pressure. A different type of experimental data, “three-phase equilibrium”, where liquid water is present in addition to vapor and solid salt, is also available in literature [3]. According to Gibbs’ phase rule, the addition of liquid water to the vapor-solid system is simply introducing an extra constraint to the system so the pressure and temperature cannot be considered independent anymore. However, once the pressure and temperature are established for the vapor-liquid-solid equilibrium, the concentration of salt in vapor can still be calculated using Eq. (13), so the results of this work are directly applicable. On the other hand, the results of the present work are not directly applicable in situations where there is a vapor-liquid equilibrium in the absence of solid salt [3], as one would need to additionally supply a model to evaluate the salt activity in liquid water as a function of pressure, temperature and the salt concentration.

## Acknowledgments

This work was supported by Los Alamos National Laboratory (LANL) Directed Research and Development funds. This research used resources provided by the Los Alamos National Laboratory Institutional Computing Program, which is supported by the U.S. Department of Energy National Nuclear Security Administration under Contract No. 89233218CNA000001. K.A.V. is grateful to Sergei Ivanov (Center for Integrated Nanotechnologies) for the discussion on nature of bonding in clusters.

## References

- [1] J. F. Galobardes, D. R. Van Hare, and L. B. Rogers. Solubility of sodium chloride in dry steam. *J. Chem. Eng. Data*, 26:363–366, 1981.
- [2] K. S. Pitzer. Thermodynamics of sodium chloride solutions in steam. *J. Phys. Chem.*, 87:1120–1125, 1983.
- [3] J. L. Bischoff, R. J. Rosenbauer, and K. S. Pitzer. The system NaCl-H<sub>2</sub>O: Relations of vapor-liquid near the critical temperature of water and of vapor-liquid-halite from 300 to 500°C. *Geochim. Cosmochim. Acta*, 50:1437–1444, 1986.
- [4] K. S. Pitzer and R. T. Pabalan. Thermodynamics of NaCl in steam. *Geochim. et Cosmochim. Acta*, 50:1445–1454, 1986.
- [5] F. J. Armellini and J. W. Tester. Solubility of sodium chloride and sulfate in sub- and supercritical water vapor from 450–550°C and 100–250 bar. *Fluid Phase Equil.*, 84:123–142, 1993.
- [6] S. M. Archibald, A. A. Migdisov, and A. E. Williams-Jones. An experimental study of the stability of copper chloride complexes in water vapor at elevated temperatures and pressures. *Geochim. Cosmochim. Acta*, 66(9):1611–1619, 2002.
- [7] G. S. Pokrovski, J. Roux, and J.-C. Harrichoury. Fluid density control on vapor-liquid partitioning of metals in hydrothermal systems. *Geology*, 33(8):657–660, 2005.
- [8] G. S. Pokrovski, A. Yu. Borisova, and J.-C. Harrichoury. The effect of sulfur on vapor-liquid fractionation of metals in hydrothermal systems. *Earth Planet. Sci. Lett.*, 266(3–4):345–362, 2008.
- [9] Art A. Migdisov and A. E. Williams-Jones. A predictive model for metal transport of silver chloride by aqueous vapor in ore-forming magmatic-hydrothermal systems. *Geochim. Cosmochim. Acta*, 104:123–135, 2013.
- [10] A. A. Migdisov, A. Yu/ Bychkov, A. E. Williams-Jones, and V. J. van Hinsberg. A predictive model for the transport of copper by HCl-bearing water vapour in ore-forming magmatic-hydrothermal systems: Implications for copper porphyry ore formation. *Geochim. Cosmochim. Acta*, 129:33–53, 2014.
- [11] T. L. Hill. *An Introduction to Statistical Thermodynamics*. Dover Publications, Inc., New York, 1986.
- [12] D. A. McQuarrie. *Statistical Mechanics*. University Science Books, Sausalito, CA, 1st edition, 2000.
- [13] J. G. Hayden and J. P. O’Connell. A generalized method for predicting second virial coefficients. *Ind. Eng. Chem., Process Des. Dev.*, 14(3):209–216, 1975.
- [14] M. J. Frisch, G. W. Trucks, H. B. Schlegel, G. E. Scuseria, M. A. Robb, J. R. Cheeseman, G. Scalmani, V. Barone, G. A. Petersson, H. Nakatsuji, X. Li, M. Caricato, A. V. Marenich, J. Bloino, B. G. Janesko, R. Gomperts, B. Mennucci, H. P. Hratchian, J. V. Ortiz, A. F. Izmaylov, J. L. Sonnenberg, D. Williams-Young, F. Ding, F. Lipparini, F. Egidi, J. Goings, B. Peng, A. Petrone, T. Henderson, D. Ranasinghe, V. G. Zakrzewski, J. Gao, N. Rega, G. Zheng, W. Liang, M. Hada, M. Ehara, K. Toyota, R. Fukuda, J. Hasegawa, M. Ishida, T. Nakajima, Y. Honda, O. Kitao, H. Nakai, T. Vreven, K. Throssell, Jr. Montgomery, J. A., J. E. Peralta, F. Ogliaro, M. J. Bearpark, J. J. Heyd, E. N. Brothers, K. N. Kudin, V. N. Staroverov, T. A. Keith, R. Kobayashi, J. Normand, K. Raghavachari, A. P. Rendell, J. C. Burant, S. S. Iyengar, J. Tomasi, M. Cossi, J. M. Millam, M. Klene, C. Adamo, R. Cammi, J. W. Ochterski, R. L. Martin, K. Morokuma, O. Farkas, J. B. Foresman, and D. J. Fox. Gaussian 16 Revision C.01, 2016.
- [15] K. D. Dahm and D. P. Visco Jr. *Fundamentals of Chemical Engineering Thermodynamics*. Cengage Learning, Stamford, CT, USA, 2015.
- [16] A. M. Hofmeister. IR spectroscopy of alkali halides at very high pressures: Calculation of equation of state and of the response of bulk moduli to the B1-B2 phase transition. *Phys. Rev. B*, 56(10):5835–5855, 1997.
- [17] W. Wagner and A. Pruss. The IAPWS formulation 1995 for the thermodynamic properties of ordinary water substance for general and scientific use. *J. Phys. Chem. Ref. Data*, 31(2):387–535, 2002.
- [18] J. J. Gomez Romera. Python implementation of standards from

the international association for the properties of water and steam.

- [19] K. H. Lemke and T. M. Seward. Solvation processes in steam: Ab initio calculations of ion-solvent structures and clustering equilibria. *Geochim. Cosmochim. Acta*, 72(14):3293–3310, 2008.
- [20] E. S. Machlin. *An Introduction to Aspects of Thermodynamics and Kinetics Relevant to Materials Science*. Elsevier, Oxford, UK, 3 edition, 2007.
- [21] J. Frenkel. A general theory of heterophase fluctuations and pretransition phenomena. *J. Chem. Phys.*, 7(7):538–547, 1939.
- [22] B. Ruscic. Active thermochemical tables: water and water dimer. *J. Phys. Chem. A*, 117(46):11940–11953, 2013.
- [23] R. G. Parr and W. Yang. *Density Functional Theory of Atoms and Molecules*. Oxford University Press, Oxford, UK, 1989.
- [24] A. Becke. Density-functional thermochemistry III. The role of exact exchange. *J. Chem. Phys.*, 98:5648–5652, 1993.
- [25] C. Lee, W. Wang, and R. G. Parr. Development of the Colle-Salvetti correlation energy formula into a functional of the electron density. *Phys. Rev. B*, 37:785–789, 1988.
- [26] J. W. Ochterski. Thermochemistry in Gaussian. *Gaussian, Inc.*, pages 1–19, 2000.
- [27] C. Ticknor, S. A. Andrews, and J. A. Leiding. Magpie: a new thermochemical code. *AIP Adv.*, (accepted), 2020.
- [28] M. W. Chase, Jr., C.A.Davies, J. R. Downey, Jr., D. J. Frurip, R. A. McDonald, and A. N. Syverud. NIST-JANAF thermochemical tables. *J. Phys. Chem. Ref. Data, Monograph 9*, pages 1–1951, 1998.
- [29] L Pankratz. *Thermodynamic Properties of Halides*. U.S. Dept. of the Interior, Bureau of Mines, Washington, DC, 1984.
- [30] P. Atkins and J. de Paula. *Atkins Physical Chemistry*. W. H. Freeman and Company, New York, 8 edition, 2006.
- [31] R. Fletcher. *Practical Methods of Optimization*. John Wiley & Sons, New York, 2 edition, 1987.
- [32] T. Driesner and C. A. Heinrich. The system H<sub>2</sub>O-NaCl. part I: Correlation formulae for phase relations in temperature-pressure-composition space from 0 to 1000°C, 0 to 5000 bar, and 0 to 1 X<sub>NaCl</sub>. *Geochim. Cosmochim. Acta*, 71(20):4880–4901, 2007.
- [33] T. Driesner. The system H<sub>2</sub>O-NaCl. part II: Correlations for molar volume, enthalpy, and isobaric heat capacity from 0 to 1000°C, 1 to 5000 bar, and 0 to 1 X<sub>NaCl</sub>. *Geochim. Cosmochim. Acta*, 71(20):4902–4919, 2007.
- [34] T. Driesner. SoWat NaCl-H<sub>2</sub>O fluid properties.
- [35] I. Persson. Hydrated metal ions in aqueous solution: How regular are their structures? *Pure Appl. Chem.*, 82(10):1901–1917, 2010.
- [36] Y. Mei, W. Liu, A. A. Migdisov, J. Brugger, and A. E. Williams-Jones. CuCl complexation in the vapor phase: Insights from ab initio molecular dynamics simulations. *Geofluids*, 2018:1–12, 2018.
- [37] J. D. Jackson. *Classical Electrodynamics*. Wiley, New York, 3 edition, 1998.
- [38] A. K. Shechekin, M. S. Kshevetskiy, and V. B. Warshavsky. The macroscopic effects of internal and external electric fields on profile and thermodynamics of a dielectric droplet. *Aerosol Sci. Technol.*, 36(3):318–328, 2002.
- [39] A. Anderko and K. S. Pitzer. Equation-of-state representation of phase equilibria and volumetric properties of the system NaCl-H<sub>2</sub>O above 573 K. *Geochim. Cosmochim. Acta*, 57:1657–1680, 1993.

## Appendix A. Equilibrium Constants

In this section we give the numerical values for the common logarithm of the equilibrium constants for the reaction  $X(\text{cr}) + n\text{H}_2\text{O} \rightarrow X:(\text{H}_2\text{O})_n$ . Tables A.9 and A.10 give data for the sodium and copper chlorides, respectively. Equilibrium constants are defined as  $K_n = e^{-\Delta\tilde{G}_{1,n}^\circ/RT}$  and the values in the tables are  $\log_{10} K_n(T)$ .

$n$	Temperature (°C)							
	100	150	200	250	300	350	400	450
0	-24.005	-20.218	-17.244	-14.848	-12.879	-11.233	-9.837	-8.639
1	-20.953	-18.125	-15.891	-14.081	-12.584	-11.325	-10.252	-9.325
2	-18.385	-16.460	-14.921	-13.660	-12.605	-11.709	-10.935	-10.261
3	-16.302	-15.222	-14.333	-13.584	-12.942	-12.382	-11.888	-11.447
4	-14.704	-14.411	-14.127	-13.854	-13.594	-13.346	-13.109	-12.883
5	-13.591	-14.028	-14.304	-14.470	-14.562	-14.600	-14.599	-14.570
6	-12.962	-14.072	-14.862	-15.432	-15.845	-16.144	-16.358	-16.507
7	-12.708	-14.447	-15.716	-16.660	-17.372	-17.912	-18.323	-18.636
8	-12.532	-14.890	-16.632	-17.945	-18.950	-19.727	-20.333	-20.806
9	-12.417	-15.388	-17.596	-19.273	-20.568	-21.579	-22.376	-23.008
10	-12.365	-15.940	-18.609	-20.646	-22.226	-23.469	-24.454	-25.242
11	-12.374	-16.547	-19.671	-22.062	-23.925	-25.395	-26.567	-27.508
12	-12.445	-17.209	-20.782	-23.523	-25.664	-27.358	-28.713	-29.805
13	-12.579	-17.925	-21.941	-25.028	-27.443	-29.358	-30.894	-32.135
14	-12.774	-18.695	-23.149	-26.577	-29.262	-31.396	-33.109	-34.497
15	-13.030	-19.521	-24.406	-28.170	-31.122	-33.470	-35.359	-36.890
16	-13.349	-20.400	-25.712	-29.808	-33.022	-35.582	-37.642	-39.316
17	-13.730	-21.335	-27.067	-31.489	-34.963	-37.730	-39.960	-41.773
18	-14.172	-22.324	-28.471	-33.215	-36.943	-39.916	-42.313	-44.262
19	-14.677	-23.367	-29.923	-34.984	-38.964	-42.139	-44.699	-46.783
20	-15.243	-24.465	-31.424	-36.798	-41.025	-44.398	-47.120	-49.337
21	-15.871	-25.618	-32.974	-38.656	-43.127	-46.695	-49.575	-51.922
22	-16.561	-26.825	-34.572	-40.558	-45.269	-49.029	-52.065	-54.539
23	-17.313	-28.086	-36.220	-42.505	-47.451	-51.400	-54.589	-57.188
24	-18.127	-29.403	-37.916	-44.495	-49.673	-53.808	-57.147	-59.868
25	-19.002	-30.774	-39.661	-46.530	-51.936	-56.252	-59.739	-62.581

Table A.9: Common logarithm ( $\log_{10}$ ) of  $K_n = e^{-\Delta\tilde{G}_{1,n}^\circ/RT}$  for NaCl. The dependence of  $\Delta\tilde{G}_{1,n}^\circ$  on  $n$  and temperature is evaluated using the parameters in Table 5 and the first numerical column in Table 2.



$n$	Temperature (°C)							
	100	150	200	250	300	350	400	450
0	-24.217	-20.453	-17.501	-15.127	-13.177	-11.549	-10.171	-8.990
1	-15.660	-13.441	-11.691	-10.276	-9.107	-8.126	-7.291	-6.571
2	-15.736	-14.042	-12.690	-11.583	-10.659	-9.873	-9.196	-8.606
3	-15.895	-14.717	-13.755	-12.950	-12.264	-11.669	-11.148	-10.684
4	-16.084	-15.417	-14.842	-14.337	-13.888	-13.483	-13.115	-12.778
5	-16.302	-16.143	-15.953	-15.746	-15.531	-15.315	-15.099	-14.886
6	-16.549	-16.895	-17.086	-17.175	-17.194	-17.164	-17.099	-17.010
7	-16.825	-17.673	-18.243	-18.625	-18.875	-19.030	-19.115	-19.149
8	-17.131	-18.476	-19.423	-20.096	-20.575	-20.914	-21.148	-21.302
9	-17.465	-19.305	-20.625	-21.587	-22.295	-22.815	-23.196	-23.471
10	-17.829	-20.160	-21.851	-23.100	-24.033	-24.734	-25.261	-25.655
11	-18.222	-21.040	-23.100	-24.633	-25.791	-26.671	-27.342	-27.854
12	-18.645	-21.947	-24.371	-26.188	-27.567	-28.624	-29.439	-30.068
13	-19.096	-22.879	-25.666	-27.763	-29.362	-30.596	-31.553	-32.297
14	-19.577	-23.837	-26.984	-29.358	-31.177	-32.585	-33.682	-34.541
15	-20.087	-24.820	-28.325	-30.975	-33.010	-34.591	-35.828	-36.800
16	-20.626	-25.830	-29.689	-32.613	-34.863	-36.615	-37.990	-39.074
17	-21.194	-26.865	-31.076	-34.271	-36.734	-38.656	-40.168	-41.364
18	-21.792	-27.926	-32.486	-35.950	-38.625	-40.715	-42.363	-43.668
19	-22.419	-29.013	-33.919	-37.650	-40.535	-42.791	-44.573	-45.988
20	-23.075	-30.125	-35.375	-39.371	-42.463	-44.885	-46.800	-48.322
21	-23.760	-31.263	-36.854	-41.113	-44.411	-46.997	-49.043	-50.672
22	-24.475	-32.427	-38.357	-42.875	-46.377	-49.125	-51.302	-53.037
23	-25.218	-33.617	-39.882	-44.659	-48.363	-51.272	-53.577	-55.417
24	-25.991	-34.833	-41.430	-46.463	-50.368	-53.435	-55.869	-57.811
25	-26.793	-36.074	-43.001	-48.288	-52.391	-55.617	-58.176	-60.221

Table A.10: Common logarithm ( $\log_{10}$ ) of  $K_n = e^{-\Delta\tilde{G}_{1,n}^\circ/RT}$  for CuCl. The dependance of  $\Delta\tilde{G}_{1,n}^\circ$  on  $n$  and temperature is evaluated using the parameters in Table 8 and the third numerical column in Table 2.